The association of hydrogen with sulfur on Mars across latitudes, longitudes, and compositional extremes

Suniti Karunatillake, James J. Wray, Olivier Gasnault, Scott M. Mclennan, A. Deanne Rogers, Steven W. Squyres, William V. Boynton, J. R. Skok, Nicole E. Button, Lujendra Ojha

AGU PUBLICATIONS

JGR

Journal of Geophysical Research: Planets

RESEARCH ARTICLE
10.1002/2016JE005016

Key Points:
- Unique Mars Odyssey GRS insight into bulk soil hydration at decimeter depth
- Limited H_2O in soil-atmosphere exchange and recharge may control salt hydration
- H_2O and S chemically associated in the South, with Fe sulfates as key minerals

Supporting Information:
- Supporting Information S1

Correspondence to:
S. Karunatillake,
wk43@cornell.edu

Citation:
Karunatillake, S., J. J. Wray, O. Gasnault, S. M. McLennan, A. Deanne Rogers, S. W. Squyres, W. V. Boynton, J. R. Skok, N. E. Button, and L. Ojha (2016), The association of hydrogen with sulfur on Mars across latitudes, longitudes, and compositional extremes, *J. Geophys. Res. Planets*, *121*, 1321–1341, doi:10.1002/2016JE005016.

Received 16 FEB 2016
Accepted 30 JUN 2016
Accepted article online 5 JUL 2016
Published online 22 JUL 2016

The association of hydrogen with sulfur on Mars across latitudes, longitudes, and compositional extremes

Suniti Karunatillake[1], James J. Wray[2], Olivier Gasnault[3,4], Scott M. McLennan[5], A. Deanne Rogers[5], Steven W. Squyres[6], William V. Boynton[7], J. R. Skok[1,8], Nicole E. Button[1], and Lujendra Ojha[2]

[1]Geology and Geophysics, Louisiana State University, Baton Rouge, Louisiana, USA, [2]Earth and Atmospheric Sciences, Georgia Institute of Technology, Atlanta, Georgia, USA, [3]Université de Toulouse [UPS; OMP; IRAP], Toulouse, France, [4]CNRS [UMR 5277], Institut de Recherche en Astrophysique et Planétologie, Toulouse, France, [5]Department of Geosciences, Stony Brook University, Stony Brook, New York, USA, [6]Department of Astronomy, Cornell University, Ithaca, New York, USA, [7]Department of Planetary Sciences, University of Arizona, Tucson, Arizona, USA, [8]SETI Institute, Mountain View, California, USA

Abstract Midlatitudinal hydrated sulfates on Mars may influence brine pH, atmospheric humidity, and collectively water activity. These factors affect the habitability of the planetary subsurface and the preservation of relict biomolecules. Regolith at grain sizes smaller than gravel, constituting the bulk of the Martian subsurface at regional scales, may be a primary repository of chemical alteration, mechanical alteration, and biosignatures. The Mars Odyssey Gamma Ray Spectrometer with hundreds of kilometers of lateral resolution and compositional sensitivity to decimeter depth provides unique insight into this component of the regolith, which we call soil. Advancing the globally compelling association between H_2O and S established by our previous work, we characterize latitudinal variations in the association between H and S, as well as in the hydration state of soil. Represented by H_2O:S molar ratios, the hydration state of candidate sulfates increases with latitude in the northern hemisphere. In contrast, hydration states generally decrease with latitude in the south. Furthermore, we observe that H_2O concentration may affect the degree of sulfate hydration more than S concentration. Limited H_2O availability in soil-atmosphere exchange and in subsurface recharge could explain such control exerted by H_2O on salt hydration. Differences in soil thickness, ground ice table depths, atmospheric circulation, and insolation may contribute to hemispheric differences in the progression of hydration with latitude. Our observations support chemical association of H_2O with S in the southern hemisphere as suggested by Karunatillake et al. (2014), including the possibility of Fe sulfates as a key mineral group.

1. Introduction

The significance of H_2O to any putative extant or extinct biosphere, as well as its potential role in the chemical and physical evolution of the Martian crust both present and past [*Bishop et al.*, 2013; *Michalski et al.*, 2013], makes factors affecting the distribution of H_2O on Mars singularly important. S variation plays an equally important role as a control on inferred fluid pH, alteration environments, and water activity [*Tosca et al.*, 2008]; atmospheric-regolith S cycles and processes may dominate over epochal time scales [*Farquhar et al.*, 2000; *Halevy and Schrag*, 2009]; analogous environments on Earth suggest atmospheric controls on S-cycles [*Peng et al.*, 2014; *Szynkiewicz et al.*, 2014].

Recent identification of sulfates as minerals important to the presence of chemically bound H_2O both by in situ [*Clark et al.*, 2005; *Johnson et al.*, 2007; *Lane et al.*, 2008; *Wang et al.*, 2008; *Wang and Ling*, 2011] and orbital [*Gendrin et al.*, 2005; *Murchie et al.*, 2009] missions motivates the search for spatial patterns to hydration state as represented by the H_2O: S molar ratio in our previous work [*Karunatillake et al.*, 2014]. Hydrated sulfates were discovered in the southern high latitudes using CRISM. Spatial patterns in hydration may also clarify ambiguities on the dependence of midlatitudinal H distribution on other hydrates [*Feldman et al.*, 2005; *Murchie et al.*, 2009; *Noe Dobrea et al.*, 2010] or on thermodynamically unstable, yet extant, subsurface ice deposits [*Jakosky et al.*, 2005]. Key processes that influence hydration likely operate in regolith constituents [*McSween et al.*, 2010], rather than outcrops and bedrock, much of which may also be mobile [*Bridges et al.*, 2012] under eolian conditions and support the formation of brine films. For this work, as before [*Karunatillake et al.*, 2014], we term corresponding regolith constituents, typically no larger than cobbles on the Wentworth scale, as bulk soil following the planetary soil definition [*Certini and Ugolini*, 2013] applied with a narrow scope [*Karunatillake et al.*, 2007]. This also ensures consistency with recent work on Mars

[*Haskin et al*., 2005; *Morris et al*., 2006; *Newsom et al*., 2007; *Wang et al*., 2009; *McGlynn et al*., 2011; *Meslin et al*., 2013; *Schröder et al*., 2014; *Fedo et al*., 2015].

Recently, *Ojha et al.* [2015] reported that perchlorate and chlorate salts are the spectrally dominant hydrated phases in infrared observations of active recurring slope lineae (RSL), seasonal dark streaks that form on sufficiently warm slopes in the Martian midlatitudes [*McEwen et al*., 2011, 2014]. Perchlorates are extremely soluble, deliquescent, and effective freezing point depressants, and therefore, their evaporitic concentration from metastable brines at the modern surface is plausible. Perchlorates have also been detected in situ by Phoenix [e.g., *Hecht et al*., 2009] and inferred by Curiosity [e.g., *Glavin et al*., 2013] and through reanalysis of Viking Lander data [*Navarro- González et al*., 2010]. But Cl abundances in bulk soils appear globally lower than S abundances [cf. *Boynton et al*., 2007; *King and McLennan*, 2010] and the RSL in which perchlorates might be locally more important as H_2O carriers are both transient and extremely limited in spatial distribution.

Chemical signatures at the Mars Odyssey Gamma Ray and Neutron Spectrometers' (GRS) lateral resolution arise as a complex function of soil, outcrop, and bedrock compositions [*Squyres and Evans*, 1992; *Diez et al*., 2009]. Corresponding calibration assessments at landing sites of four previous missions (Viking, Pathfinder, and Mars Exploration Rovers) by *Karunatillake et al.* [2007] indicate that the bulk soil may dominate compositional signatures. This applies even in the southern hemisphere of Mars, where regional rock areal fractions exceed the ~20% maximum observed at the northerly landing sites. The aqueous mobility of H_2O and S may also enhance their distribution in soil, which offers greater surface area for the capillary flow of brines.

Unlike the GRS, most remote sensing observations of Mars are sensitive only to tens of micron depths [*Christensen et al*., 2004; *Poulet et al*., 2007] or less and focus on local outcrops and bedrock [e.g., *Murchie et al*., 2009]. The GRS, with hundreds of kilometers scale of lateral resolution and decimeter-scale depth sampling throughout the midlatitudes, fills the resulting gap in knowledge of H_2O and S association in the bulk soil. In addition, it also provides a more global understanding of hydrous sulfates on Mars and their genetic processes, extending the scope of current work using reflectance and emission spectroscopy [*Cloutis et al*., 2006; *Morris et al*., 2009; *Pitman et al*., 2014; *Lane et al*., 2015]. With this strength in mind, we characterize latitudinal variation in the hydration signature of bulk soil in the Martian midlatitudes for insight into the nature of hydration using H_2O and S trends. For brevity, we refer to the stoichiometric H_2O: S molar ratio as "hydration state" throughout this manuscript.

The variability of hydration due to thermodynamic stability [*Feldman et al*., 2005; *Steiger et al*., 2011], due to diversity of sulfate minerals as determined remotely [*Murchie et al*., 2009], and due to diversity observed in situ [e.g., *Yen et al*., 2008] may obscure any association between H_2O and S. Additionally, ice tables detected within ~ 1 m depth at latitudes as low as 45° [*Byrne et al*., 2009] suggest a complex interplay among scattered ice bodies at depth and various water-bearing material at shallower levels including clay, zeolite, and silica [*Jouglet et al*., 2007; *Bishop et al*., 2009; *Wray et al*., 2009]. Several of these hydrous sulfate minerals were first identified by *Ehlmann et al.* [2009]. The GRS is sensitive to some of the ice table variation as it samples the surface to several decimeter depths. Such depths, relative to the tens of microns sensitivity of visible, near-infrared, and thermal infrared (VNTIR) instruments, may reveal compositional differences at the surface. Hints of this possibility also arise from in situ observations at Gusev Crater where Paso Robles type soil, rich in Fe sulfates, sometimes underlies "typical" Martian basaltic soil [*Yen et al*., 2008]. Furthermore, recent laboratory work reinforces the possibility of amorphous sulfates, in general, and amorphous Fe sulfates in particular, in Martian bulk soil as suggested in situ at Gale Crater [*Sklute et al*., 2015]. Despite such complexities, our prior paper [*Karunatillake et al*., 2014] suggests a compelling association of H_2O with S, consistent with hydrous Fe^{3+} sulfate distribution at global scales, especially in the southern hemisphere.

This work develops the initial insight offered by our previous paper [*Karunatillake et al*., 2014]. Accordingly, we first assess the latitudinal variation in hydration state given the latitudinal correspondence of H_2O(s) thermodynamic stability [*Feldman et al*., 2004] and of the planetary dichotomy in surface elevation. These may represent meaningful differences in climate conditions that control the atmosphere-surface interface and resultant soil composition. Next, we compare hydration states across H_2O and S enrichment and depletion regions to ascertain which component, H_2O or sulfate, controls the hydration state [*Wang et al*., 2006; *Milliken et al*., 2007]. The regional scope of our work is assisted in particular by the GRS's intrinsic spatial resolution of roughly 440 km [*Boynton et al*., 2007; *Karunatillake et al*., 2007], complementing the local chemistry [*Bishop et al*., 2009] of VNTIR remote sensing missions. As a key assessment of our previous work

[*Karunatillake et al*., 2014], we also investigate whether the apparent spatial association of H and S reflects spatial autocorrelation and precision issues more than ground truth.

2. Data and Methods

We use elemental mass fraction data, derived from GRS γ photon spectra as discussed by *Boynton et al.* [2007], corresponding to the cumulative spectra through 2009. These data are limited to between roughly ±60° latitude since, as *Boynton et al.* [2007] discuss, accurate mass fractions are difficult to calculate within the polar regions with the exception of H_2O. While the relatively low intensity of characteristic peaks for S makes the mass fraction map difficult to generate, spectra accumulated during science operations enabled the first such midlatitudinal map to be created [*King and McLennan*, 2010]. Nevertheless, substantial smoothing necessary to achieve sufficient numerical precision causes spatial autocorrelation [*Karunatillake et al*., 2012] and limits the spatial resolution of the S mass fraction map. Therefore, we utilized $10° \times 10°$ bins for the S mass fraction, $w(S)$, data set. Consequently, we rebinned $w(H_2O)$ from its original $5° \times 5°$ resolution to $10° \times 10°$. While this reduced the number of data by a factor of 4, substantially increasing apparent uncertainties in regression parameters, reporting higher uncertainties was preferable to the alternative of hidden and poorly quantified errors of spatial autocorrelation [e.g., *Karunatillake et al*., 2012]. Generally, spatial autocorrelation causes reported values to be numerically similar solely due to spatial proximity as opposed to geological or geochemical processes, which in turn reduces the degrees of freedom in data [e.g., *Karunatillake et al*., 2012].

We map the global hydration state distribution by first computing the moles of H_2O, $n(H_2O)$, and of S, $n(S)$, in 100 g of soil at each $10° \times 10°$ bin. This takes the form $w(H_2O) \times 0.0555$ employing standard atomic mass values [e.g., *Wieser*, 2006]. Similarly, $w(S) \times 0.0312$ yields the S moles. The molar ratio is computed subsequently, with corresponding uncertainty propagated as $\frac{n(H_2O)}{n(S)} \sqrt{\left[\frac{\sigma_m\{w(S)\}}{w(S)}\right]^2 + \left[\frac{\sigma_m\{w(H_2O)\}}{w(H_2O)}\right]^2}$, where σ_m denotes the standard error of each variable. We use mass fractions in the radical, since the factor that converts the mass fraction and its standard error to moles cancels for each ratio term. The molar ratio and corresponding uncertainty maps underpin our analyses.

With our recent work [*Karunatillake et al*., 2014] demonstrating a compelling association between H_2O and S at hemispheric scales, we proceed to evaluate any latitudinal trends in the hydration state. Optimizing between spatial precision and numerical uncertainty, we used 10° wide latitudinal bands northward and southward of ±10°. The 20° wide equatorial band from $-10°$ to 10° acted as the reference to compare northern variations with their southern counterparts. We compute the average and standard deviation of the hydration state distribution within each band, assessed in more detail subsequently with frequency histograms. We compare typical hydration values suggested by these analyses with those of sulfate minerals confirmed or suggested on Mars as described in the subsequent sections. Within each latitudinal band, this helps to identify which sulfates could act as primary carriers of hydration in bulk soil, advancing the initial insight from our previous work [*Karunatillake et al*., 2014]. To prevent misleading outcomes from the hydration state alone, we reinforce our analysis with regression results, examples of which we discuss in section 3.4.

The hydration state frequency histograms we use all derive from kernel density estimate (KDE) processing, yielding probability density values. The superiority of this method relative to raw histograms stems from the properties of KDE. For example, peaks in the distribution can be distinguished visually above noise. KDE prevents additional common weaknesses of traditional histograms: discontinuity artifacts and dependence on end points of bins. Equally important, KDE does not involve averaging the data geospatially. Instead, the KDE kernel serves as a means to characterize the shape of a distribution without relying on the simplistic mean and standard deviation parameters typically used in the literature. As a nonparametric method, KDE also reveals the nature of the overall distribution without bias from assumed population distributions. Consequently, skewness, kurtosis, multimodality, and other deviations from normal distributions (i.e., Gaussian or random normal) become identifiable visually. While still an emerging analytical method in planetary science [e.g., *Gasnault et al*., 2010] for enhanced insight into spatial data, KDE remains both critical and mature in fields as diverse as signal processing [*Liu et al*., 2009], econometrics [*Bouezmarni and Scaillet*, 2005], automated visual surveillance [*Elgammal et al*., 2002], and neuroscience [*Shimazaki and Shinomoto*, 2010].

We adapted a standard KDE plot algorithm by *Hamrick* [2008] to identify subdistributions uniformly at a given bandwidth across data of varying dynamic range. This effectively bins the data at infinitesimal increments by using a bandwidth parameter (w). Many analysts optimize the bandwidth (w) by computationally [*Sheather and Jones*, 1991] identifying a value that minimizes the asymptotic mean integrated squared error. We instead relied on the more laborious, yet robust, method of varying w continuously between the minimum, 0.2, and maximum, 2, to identify the optimal value. As used in the following equation, w serves a role analogous to bin width in traditional frequency histograms. The KDE function took the form $f_w(y) = \frac{1}{nw}\sum_{j=1}^{n} K\left(y - y_j \Big/ w\right)$, with n the number of data and K the kernel. Given its simplicity and established nature, we relied primarily on a Gaussian kernel, of form $K\left(y - y_j \Big/ w\right) = \frac{1}{w\sqrt{2\pi}} \exp\left[-\frac{(y-y_j)^2}{2w^2}\right]$.

As presented in section 3.1, comparison of outcomes with other kernels, including triangular, uniform, and triweight, also suggested more informative results from the Gaussian kernel. Where the KDE histogram resembles a Gaussian distribution, we also quantify the values between 10th and 90th percentiles to approximate 80% of the surface area and in turn the typical hydration range within a given latitudinal band. The latitudinal band sizes we use minimized biases that would result from variations in the area of pixels. Even where the distributional shape disallows direct translation to surface area, distinct peak values and shoulders can suggest representative bulk soil hydration states.

2.1. Comprehensive Candidate Hydrous Sulfate Library

We compare representative hydration states with a comprehensive mineral library of various hydrous as well as hydroxylated sulfates that may reasonably be expected on Mars. Our prior work [*Karunatillake et al.*, 2014] establishes the utility of restricting the library to hydrous sulfates, resulting primarily from a compelling association between H and S. As before, our results establish consistency with, rather than proof of, specific hydrous sulfate phases, particularly given how high abundances of anhydrous sulfates could skew the observed distributions.

We develop the mineral library on the basis of peer-reviewed literature on remote sensing and in situ observations [e.g., *Clark et al.*, 2005; *Gendrin et al.*, 2005; *Johnson et al.*, 2007; *Lane et al.*, 2008; *Murchie et al.*, 2009; *Yen et al.*, 2008; *Wang et al.*, 2008; *Wang and Ling*, 2011; *Wray et al.*, 2010], thermodynamic [e.g., *Steiger et al.*, 2011] and climatic models [e.g., *Halevy et al.*, 2007], hydration-dehydration experiments that simulate Martian conditions [*Xu et al.*, 2009], and meteoritic observations [*Righter et al.*, 2009]. These observations, models, and experiments place candidate minerals in several overlapping categories, with an extensive review of the literature provided in the supporting information : bulk soil observed in situ (supporting information section 1); outcrop and bedrock sensed remotely or in situ (section 2); thermodynamic feasibility (section 3); and tentative possibilities (section 4). The nature of gamma photon spectra indicating elemental composition at regional scale makes the judicious selection of minerals essential; a merely exhaustive list of all terrestrial and laboratory minerals would undermine effective modeling.

2.2. Mineral Library and Methodology Summarized

Among the hydrous sulfate candidates we assessed to include in our library, 27 appear promising as described in sections 1–4 of the supporting information and enumerated alphabetically in Table 1. These yield 13 distinct hydration states that we compare with those suggested by the peaks in the KDE plots of GRS-derived hydration states. Despite substantial overlap in possible hydration states across the mineral groups (Table 1), Mg sulfates are generally not hydrated in the 2.5 to 4 range with the exception of starkeyite at 4 [*Steiger et al.*, 2011]; even amorphous meta-table forms of Mg sulfates may not exceed a hydration state of 3 [*Wang et al.*, 2009] and are thermodynamically more likely to be hydrated at 1–2 [*Steiger et al.*, 2011]. While additional minerals will continue to be proposed in the future, our literature search was sufficiently thorough and resulting library sufficiently broad to reliably capture patterns in hydration state.

After assessing the latitudinal variation in hydration state, we compare hydration across H_2O and S enrichment and depletion regions. This enables us to determine the significance of H_2O—relative to the sulfate component in minerals—as the control on hydration state. Regions of enrichment and depletion are delineated at a significance exceeding one standard deviation while simultaneously accounting for numerical

Table 1. Library of Candidate Hydrous Sulfate Phases Used in This Work Listed Alphabetically[a]

Name	Formula	Hydration state	Significance Section
Alunite	$KAl_3(SO_4)_2(OH)_6$	1.5	2
Amarantite	$Fe_2O(SO_4)_2.7H_2O$	3.5	1
Amorphous Mg sulfate	$MgSO_4.H_2O$	1	2 and 3
Amorphous Mg sulfate	$MgSO_4.2H_2O$	2	2 and 3
Bassanite	$CaSO_4.1/2H_2O$	0.5	2
Bilinite	$Fe(II)Fe(III)_2(SO_4)_4.22H_2O$	5.5	3
Butlerite	$Fe(SO_4)(OH).2H_2O$	2.5	1
Copiapite	$Fe(II)Fe(III)_4(SO_4)_6(OH)_2.20H_2O$	3.5	2 and 3
Epsomite	$MgSO_4.7H_2O$	7	1 and 3
Ferric sulfate hydroxide	$FeSO_4OH$	0.5	2
Ferricopiapite	$(Fe^{3+})_{2/3}(Fe^{3+})_4(SO_4)_6(OH)_2.20H_2O$	3.5	1
Fibroferrite	$Fe(SO_4)(OH).5H_2O$	5.5	1
Gypsum	$CaSO_4.2H_2O$	2	2
Hexahydrite	$MgSO_4.6H_2O$	6	3
Hohmannite	$Fe_2O(SO_4)_2.8H_2O$	4	1
Jarosite species	$KFe_3(SO_4)_2(OH)_6$	1.5	2
Kieserite	$MgSO_4.H_2O$	1	2 and 3
Kornelite	$Fe_2(SO_4)_3.7H_2O$	2.33	1
Kornelite	$Fe_2(SO_4)_3.8H_2O$	2.67	1
Magnesiocopiapite	$MgFe_4(SO_4)_6(OH)_2.20H_2O$	3.5	1
Metahohmannite	$Fe_2(SO_4)_2(OH)_2.3H_2O$	2	1
Parabutlerite	$Fe(SO_4)(OH).2H_2O$	2.5	1
Pentahydrite	$MgSO_4.5H_2O$	5	3
Sanderite	$MgSO_4.2H_2O$	2	3
Starkeyite	$MgSO_4.4H_2O$	4	3
Szomolnokite	$FeSO_4.H_2O$	1	2

[a]Significance of each mineral is described in sections 1–4 of the supporting information. For cases of −OH groups in the mineral structure, we approximated the hydration state by computing H_2O molar equivalent as (number of H atoms)/2. Since the combination of H and S chemical data can only provide insight into hydrated minerals, we do not consider anhydrous phases.

uncertainties of the data as applied for chemical provinces by *Karunatillake et al.* [2009]. This threshold also satisfyingly generates regions with number of data exceeding that in any 10° wide latitudinal band.

Relatively high magnitudes of average hydration state uncertainties arise in part from the conservative $10° \times 10°$ bin size, which substantially reduces the apparent degrees of freedom. However, such uncertainties do not undermine the results and discussion that follow due to several reasons: first, key observations rely on distributional and parametric trends rather than individual values. Second, the underlying data sets manifest satisfactory signal: noise ratios, with regional-scale standard errors on the order of 5–10% of average mass fractions. Third, our enrichment and depletion regions are statistically sound [*Karunatillake et al*., 2009] and complemented by analyses over 11 latitudinal bands.

3. Results and Discussion

As developed in our recent work [*Karunatillake et al*., 2014], a compelling correlation between mass fractions, $w(H_2O)$ and $w(S)$, without excess H_2O, particularly in the southern hemisphere, makes sulfates likely phases to hydrate Martian midlatitudinal bulk soil. The absence of excess H_2O also suggests that some sulfates may remain anhydrous [*Karunatillake et al*., 2014]. Given the general absence of excess H_2O, abundant anhydrous sulfates could skew computed hydration states to lower values. This necessitates caution in associating peaks suggesting particularly low hydration states with specific minerals. Furthermore, since GRS data constrain sulfate phases by revealing the spatial relationship between H and S, we cannot identify anhydrous sulfates that may exist in bulk soil. Lastly, the likely association of GRS-derived Fe, K, Ca, and Al with non-S bearing phases, particularly silicates [*Taylor et al*., 2010], diminishes the ability of their distributions to identify likely sulfates, in turn justifying our focus on H and S. With this context in mind, we discuss our results of latitudinal variations first, which provides spatially narrow regional bands relative to the elemental enrichment and depletion regions. Second, we identify the primary elemental control on hydration state by using the enrichment and

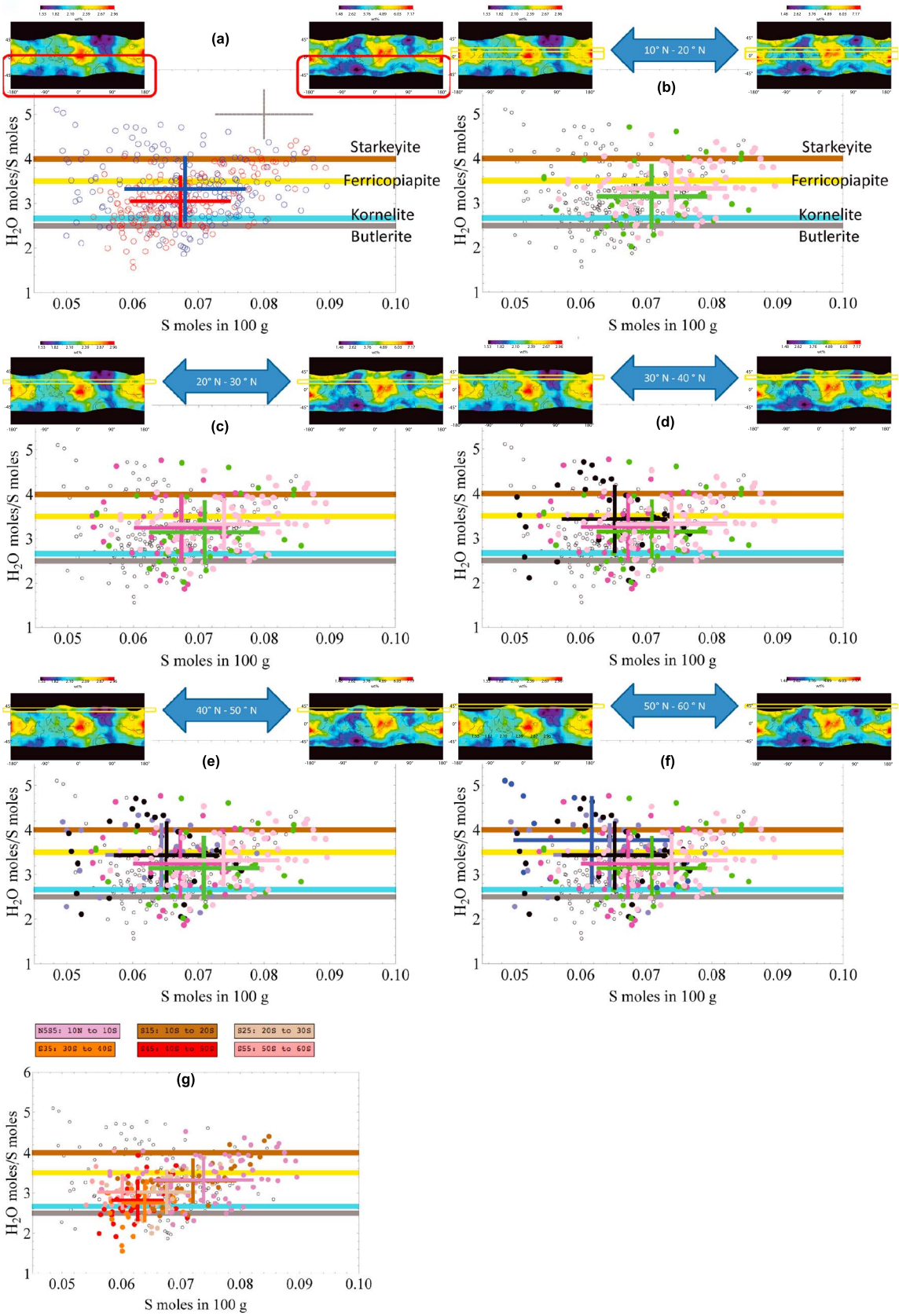
(a)
10° N - 20 ° N
(b)
20° N - 30 ° N
(c)
30° N - 40 ° N
(d)
40° N - 50 ° N
(e)
50° N - 60 ° N
(f)
(g)
Starkeyite
Ferricopiapite
Kornelite
Butlerite
H2O moles/S moles
S moles in 100 g
N58S: 10N to 10S
S15: 10S to 20S
S25: 20S to 30S
S35: 30S to 40S
S45: 40S to 50S
S55: 50S to 60S

Figure 1

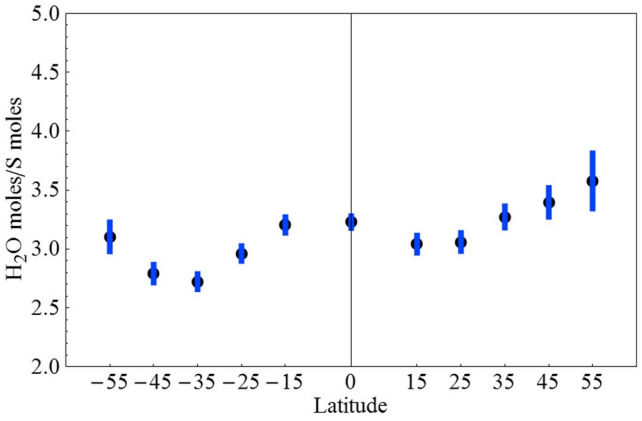

Figure 2. Hydration state plotted against latitude to identify latitudinal variations in average hydration. Blue error bars signify one standard error and the black dot indicates the average, both accounting for heteroscedasticity [*Karunatillake et al*., 2010]. Midpoint of each 10° wide latitudinal band is shown on the *x* axis. Note nearly monotonic increase in hydration state to a maximum of ~3.5 toward northerly latitudes. Hydration initially decreases toward southerly latitudes to a minimum of ~2.8, then increases.

depletion regions. Lastly, we use longitudinal analyses to assess whether the correlation between H and S may reflect artifacts and spatial autocorrelation of the data, as opposed to ground truth.

3.1. Latitudinal Trends in Hydration State

The global and hemispheric analyses in our recent work suggested that Fe^{3+} sulfates may chemically bind H_2O in bulk soil as a key hydrous sulfate species at regional spatial scales in the southern hemisphere. The reasonably sized latitudinal bands that we define in section 2 provide finer spatial context and additional detail. Four plausible sulfates—starkeyite, ferricopiapite, kornelite (i.e., assuming the 8 H_2O variety), and butlerite (Table 1)—act as illustrative references in Figure 1. The hydration states appear similarly distributed between the two hemispheres, overlapping within the means and standard deviations (Figure 1a). That said, the data suggest slightly lower hydration states in the southern hemisphere, while the northern distribution overlaps compellingly with that of the equatorial reference band (blue cross (Figure 1a) overlaps with pink cross (Figure 1b)).

Intriguingly, Figures 1b–1f show a sustained trend of increasing hydration state from less than 3.5 (e.g., between ferricopiapite and kornelite) to values exceeding 3.5 (e.g., starkeyite) within the map bounds in the northern hemisphere. Decreasing mean S concentrations accompany this trend, with a proportional decrease in average S molar content (moles per 100 g of regolith) approximating 16% relative to the equatorial band's 0.074 value (equivalent to mass fraction $0.074 \times 32.065 = 2.4\%$). This can explain the ~15% proportional increase in the hydration state from ~3.3 at the equator, without significant variation in H_2O concentration. Consequently, we infer that the H_2O concentration varies less than that of S going northward, reinforcing the hemispheric-scale decoupling between them in the north [*Karunatillake et al*., 2014].

H_2O abundances may decouple from S in the north due to a confluence of decreasing depth to ground ice stability, H_2O accumulation in pore spaces of fine particle mantles presumably thickening northward, H_2O adsorption on fine particles, and specific surface area [*Jänchen et al*., 2009; *Beck et al*., 2010]. Additional potential contributors include the proportion of amorphous phases that may adsorb H_2O [*Meslin et al*., 2013], weakening the chemical association with S. Consequently, sulfate may exert only a minor influence on the latitudinal variations in hydration states in the northern hemisphere.

Figure 1. Plots of hydration state against S moles per 100 g to identify latitudinal trends in hydration state as discussed in section 3.1. The colored bands identify example hydrous sulfates consistent with the bulk hydration range on Mars. Map of S mass fractions on left and H_2O mass fractions on right are outlined to indicate the latitudinal bands highlighted in the graphs. (a) Highlight of average hydration state and S moles/100 g in each hemisphere. The southern hemisphere is indicated in red and the northern hemisphere is indicated in blue. Cross shows the standard deviation of the distribution. For comparison, the typical numerical uncertainty of the data are shown by the gray cross as root-mean-square of uncertainty maps. (b) Green cross represents the 10–20° N band. Pink cross represents the midlatitudinal band, for reference. (c) Northerly progression of hydration state, with 20–30°N indicated in bright purple. (d) Northerly progression continued with 30–40° N indicated in black. (e) Northerly progression continued with 40–50° N indicated in lavender. (f) Northerly progression continued with 50–60°N indicated in blue. Note the apparent hydration state increase toward the northerly latitudes. (g) Complete southern trend with colors indicating each latitudinal band corresponding to their northern counterparts in Figures 1b–1f. Legend identifies the color code with N5S5 corresponding to the 10 N to 10 S latitudinal band, for example. Note the progression of decreasing hydration state toward the southern latitudes. Section 3.1 discusses the implications of these trends.

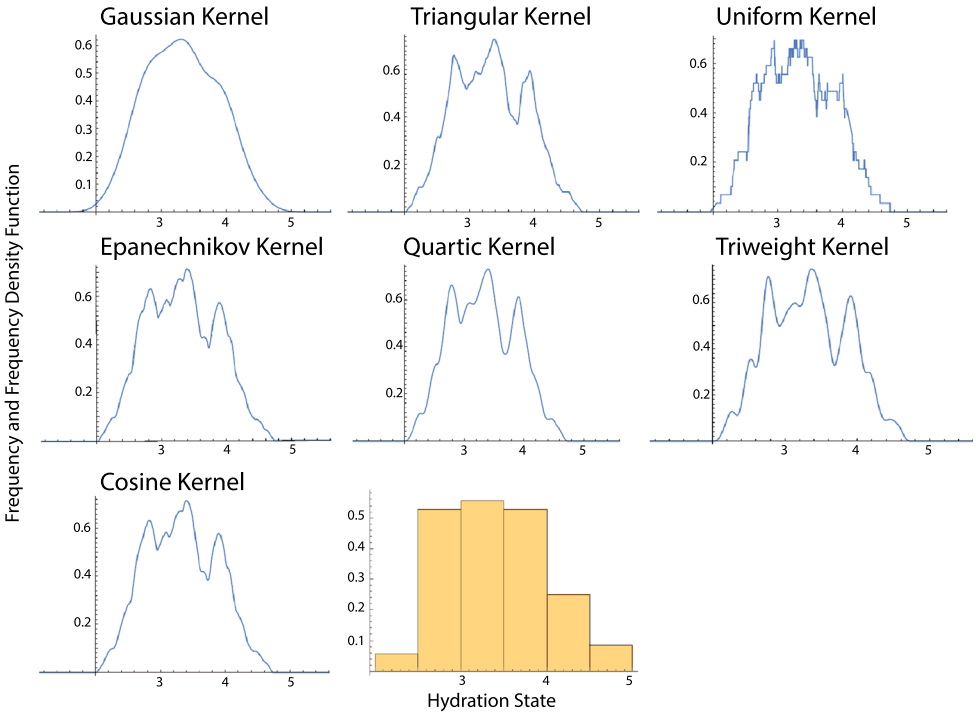

Figure 3. KDE histograms for the 5°N to 5°S latitudinal band employing Gaussian, triangular, uniform, Epanechnikov, quartic, triweight, and cosine kernels at smallest bandwidth as a comparison across the range of kernels employed with KDE. A raw histogram is also shown for comparison. Vertical axis shows KDE frequency, while the horizontal axis shows the hydration state. Among the different kernels, the uniform and Epanechnikov kernels seem more susceptible to noisiness. The fit noisiness decreases through quartic, triangular, triweight, and cosine kernels. The least noisiness, and consequently the clearest distribution shape insight, results from the Gaussian kernel. Nevertheless, all seven kernels converge broadly on the location of distributional peaks within the hydration state of 2.7–4, consistent with the Gaussian kernel's primary peak at 3.3. Section 3.2 presents the implications.

Unlike the north, hydration state generally decreases southward from the Equator (Figure 1g). With the exception of the 50°–60° latitudinal band, the hydration state decreases from the equatorial band to about 2.8 as S molar content decreases to ~0.06. The similar decrease of both hydration state and S content, by about 15%, represents a corresponding decrease in H_2O content. This relationship reinforces the compelling possibility of H_2O bound primarily in sulfates in the southern hemisphere [*Karunatillake et al.*, 2014], producing a spatially associated variation in both. We summarize the latitudinal trends in hydration state in Figure 2. Higher hydration state in the 50°–60° south band relative to much of the southern hemisphere may reflect a decoupling of S and H_2O in the polar regime of Mars, perhaps analogous to the broader trend at play in the northern hemisphere.

3.2. Optimal KDE Kernel for Mineralogic Insight From Hydration States

The inability to identify minerals uniquely remains a critical caveat of hydration states. However, once the potential for such minerals is established by complementary means—such as the regression of H_2O with S [*Karunatillake et al.*, 2014]—hydration states help to identify relevant mineral groups. Consequently, we focus on the southern hemisphere which demonstrates a stronger possibility for hydrous sulfates to bind available H_2O [*Karunatillake et al.*, 2014]. Furthermore, Figure 3 compares the KDE histograms for the 5 N to 5 S equatorial latitudinal band employing Gaussian, triangular, uniform, Epanechnikov, quartic, triweight, and cosine kernels, which helped us identify the Gaussian kernel as optimal for our work. The general shape convergence of the raw histogram further reinforces the utility of the Gaussian kernel. Specifically, the raw histogram generates only a coarse distributional shape profile, unlike any of the kernels. This comparison collectively reinforces the KDE strengths noted in section 2.1, including the ability to discern peaks in the distribution visually above noise, unlike a raw histogram, and minimization of shape dependence on bin end points.

Our results for the equatorial reference band (Figure 3) allow a detailed comparison across the different kernels. The Gaussian kernel shows an approximately unimodal distribution with hints of shoulders at 2.9 and 3.8 hydration overlapping with a peak at 3.3. The triangular kernel confirms this with a possibility of distinct peaks at 2.8, 3.4, and 3.9 hydration. The uniform kernel seems to diverge from the broader shape of the distribution, as evident in increased noisiness. However, the resulting KDE histogram remains generally consistent with dominant distributional peaks constrained between 2.7 and 4 hydration. A better-fitting Epanechnikov kernel suggests peaks at 2.8, 3.4, and 3.9 hydration, as refined by an even better fit with the quartic kernel at approximately the same peak locations. The triweight kernel reinforces the detected peaks, with tentative evidence of subpeaks and shoulders proximal to the primary peaks. Lastly, the cosine kernel reduces noise relative to the quartic kernel. Consequently, all seven kernels converge broadly on the location of distributional peaks within the 2.7 and 4 hydration state range. Meanwhile, as shown in Figure 3, the Gaussian kernel yields the least noise while revealing the primary 3.3 peak. Among our candidate minerals (Table 1), hydrous Fe sulfates match the peaked region best, even though starkeyite could contribute to the shoulder feature proximal to 4. The apparent unimodality with the Gaussian kernel does not suggest mixtures of differently hydrated phases at similar abundance in bulk soil, even though minor amounts of non-Fe sulfates could contribute to the multimodality suggested by non-Gaussian kernels and the hints of shoulders at 2.9 and 3.8 in the Gaussian kernel. Given the consistency across kernels and greater insight possible from the Gaussian kernel, we use the Gaussian kernel to characterize the remaining latitudinal bands.

3.3. Likely Mineralogy Based on Hydration State Distributions

Relative to the midlatitudinal reference band, the first southern band, from −10° to −20°, shows interesting variations. First, the Gaussian KDE shows a potential multimodality with a major peak at 3.4 hydration and a minor one at 2.7, roughly at half the frequency density (Figure 4 compiles all southern latitudinal band histograms into one panel). The KDE histogram tentatively suggests shoulders at higher hydrations of 4 and 4.7. We also infer a wider and longer distributional tail at higher values, i.e., positive skewness. This would be consistent with a substantial amount of hydrous Fe sulfates mixed with several other phases. We also infer greater compositional diversity here at hydrations above 4. The two peaks would suggest hydrous Fe sulfates for the central 3.4 value, while the lower hydration may correspond to a mixture of less hydrated Ca or Mg sulfates with more hydrous Fe sulfates (Table 1). Alternatively, two distinct Fe-sulfate phases, such as ferricopiapite and butlerite, may also explain this distribution.

Variable hydration at 4 and above could correspond to varying Mg-sulfate phases (Table 1). While we cannot exclude additional minerals or phases, the hemispherically strong association between H_2O and S [*Karunatillake et al*., 2014] supports a bulk soil hydration dominated by sulfates rather than ground ice, porosity, clays, etc., throughout the southern hemisphere. Observations by the Sample Analysis at Mars suite aboard the Curiosity Rover at Gale crater may indicate the presence of amorphous sulfates in the less than 150 μm soil component [*Archer et al*., 2014; *McAdam et al*., 2014]. If present, these phases could manifest a continuum of hydration states. While such a continuum seems less likely than crystalline minerals to yield specific shoulders in the histogram as observed by us, we cannot exclude metastable distinct adsorbed hydrations arising from soil-atmosphere processes over geologic time scales. With these thoughts applying throughout the remaining southern latitudinal bands, we clarify exceptions as needed.

In contrast to the first southern latitudinal band, the −20° to −30° latitudinal band shows a broadened peak between 2.8 and 3.4 hydration, without evidence for shoulders at higher hydration (Figure 4b). The shoulder at approximately 2.2 could arise from the presence of minor less hydrous Ca or Mg sulfates, such as gypsum (Table 1). The broadness of the peak suggests the possibility of a multimineral mix, though the hydration range corresponds mostly to Fe sulfates.

Further south at −30° to −40° latitudes, the hydration state distribution (Figure 4c) contrasts with the previous latitudinal bands in two ways: (1) the distributional shape resembles a laterally inverted distribution relative to the −10° to −20° band and (2) the primary peak dominates with more specificity in hydration than either previous band. The distributional peak suggests minerals with hydration approximating 2.8, such as any of several Fe-sulfate phases including kornelite and butlerite (Table 1). Meanwhile, the negative skewness with the longer and wider tail at lower hydration along with the shoulder at 1.9 hydration suggests the

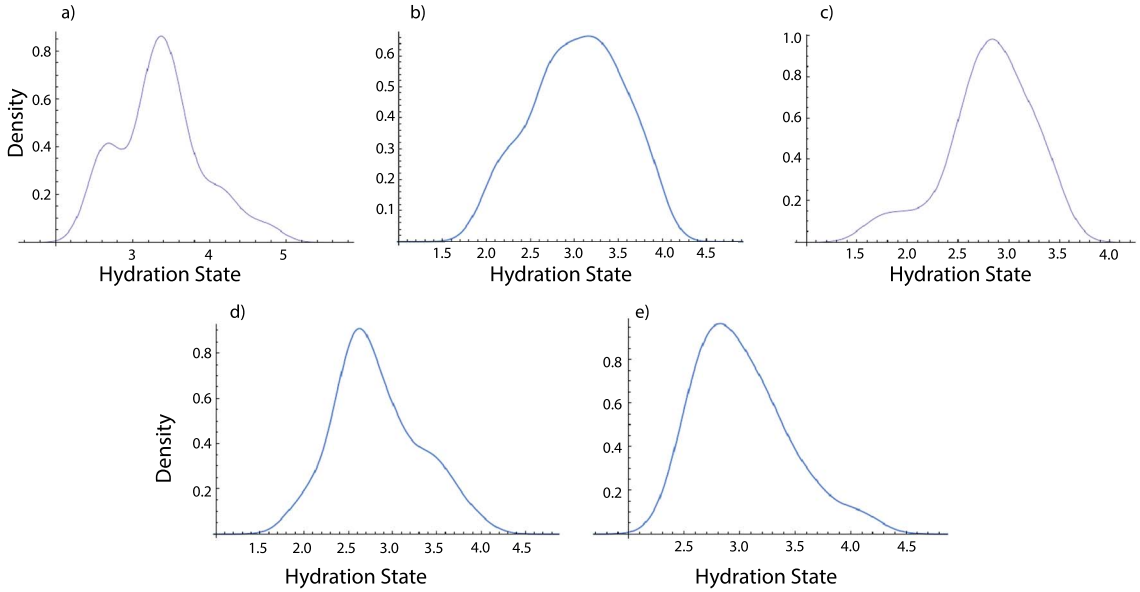

Figure 4. Histograms of hydration state variation in the southern hemisphere, partitioned into 10° wide latitudinal bands, with the first centered at − 10°, optimal for the data spatial resolution. All histograms were processed with a Gaussian KDE for the reasons discussed in section 2 and supported further in section 3.2. Latitudinal bands labeled by latitudinal extent as (a) −10 to −20, (b) −20 to −30, (c) −30 to −40, (d) −40 to −50, and (e) −50 to −60. Each band, with the exception of Figure 4e, consists of 36 data points from 10° × 10° areas. Given overlap with the southern perimeter of chemical maps, band (Figure 4e) contains 21 data. Section 3.3 presents the insight resulting from broad trends and variations across the latitudinal bands.

presence of less hydrous Mg or Ca sulfate phases such as gypsum and sanderite (Table 1). Higher hydration Mg and Ca sulfates seem inconsistent with the observed distribution.

The distribution shifts decisively to lower hydration in the −40° to −50° latitudinal band, with a distinct peak at 2.6 and a shoulder at 3.5 (Figure 4d). Nevertheless, positive skewness suggests greater abundance of hydrations above 3.5 relative to those below 2.5. Consequently, this latitudinal band diverges meaningfully from the −10° to −20° and −20° to −30° bands that have a dominant hydration approximating 3.5. The reduced 2.6 hydration may indicate Fe sulfates such as butlerite or kornelite at higher abundances than higher-hydration Fe sulfates such as ferricopiapite (Table 1). Intriguingly, the new lower hydration peak exceeds the hydration states closer to 2 that typify Mg and Ca sulfates (Table 1).

With only 21 data available, the −50° to −60° latitudinal distribution (Figure 4e) provides statistically less robust information than the higher latitudinal bands, each with 36 data points, and the equatorial reference band with 72 data points. The −50° to −60° band manifests a distinct peak at 2.8 hydration with positive skewness accompanying a shoulder at approximately 4. The peak suggests hydrous Fe sulfates, while the shoulder could represent starkeyite (Table 1) [*Ackiss and Wray*, 2014]. This latitudinal band also marks the perimeter of available mapped chemical data.

Figure 5 summarizes the mineral phases suggested by the hydration state distributions across latitudinal bands. As evident in this visual summary (Figure 5), hydration states in the southern latitudinal bands collectively show consistency with hydration by Fe sulfates. The distributions do not suggest occurrence of Mg and Ca sulfates at abundances greater than that of minor components. The broad trend, except for the lowest latitude band, converges not only with the parametric summary represented by averages and variance (Figure 2) but also with our recent work [*Karunatillake et al.*, 2014].

3.4. Geochemical Pathways for the Inferred Mineralogy

The possibility of a consistent chemical signature across the latitudes encourages us to consider processes that may associate H_2O preferentially with Fe sulfates in Martian bulk soil. We model such processes by first selecting a representative soil type. Based on our review of the current literature on Mars and Mars analog conditions (supporting information), we find Barnhill class soil, revealed by involuntary excavations at Paso Robles in Gusev Crater, best suited for this purpose. Barnhill class soil also shows remarkable enrichment

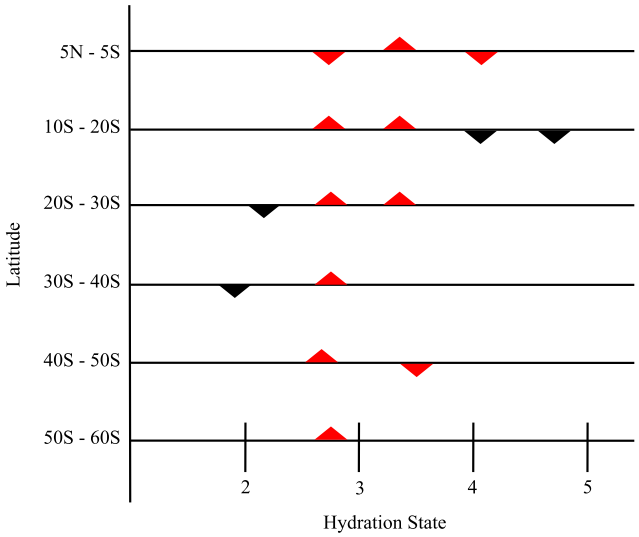

Figure 5. The hydration state variation across the southern hemisphere of Mars, summarizing the insight from probability density histograms shown in Figure 4. The horizontal axis represents the hydration state, while the vertical axis represents the latitude. Triangles identify the approximate peaks (upright triangles) and shoulders (inverted triangles) of the hydration states within each latitudinal band, as described in section 3.2. Red triangles indicate consistency with Fe^{3+} sulfates and black triangles with Ca/Mg sulfates. As shown, Fe^{3+} sulfates may occur consistently across all latitudes. The distributions do not suggest occurrence of Mg and Ca sulfates at greater abundances than minor components.

by phases consistent with hydrous Fe^{3+} sulfate as discussed in the supporting information section 1 [e.g., *Yen et al.*, 2008].

The Barnhill Class type soil suggests that two general groups of processes may yield the compositional signature we observe across Mars. First, hydrothermal processes. Proximity of Barnhill class soil to the Home Plate feature in the Columbia Hills construct suggests a meaningful role to hydrothermal activity. Phraetomagmatic activity, or at least explosive volcanism in the presence of high volatile content, may have contributed to the formation of Home Plate itself [*Lewis et al.*, 2008]. Location within the southern highlands, ancient relative to the exposed northern lowlands, suggests that any related hydrothermal processes may predate the Amazonian. Nevertheless, the intrinsically localized nature of hydrothermalism presents intriguing challenges in imparting a regional-scale signature to bulk soil.

Despite localized occurrence, hydrothermal activity may have been abundant on ancient Mars. This is also consistent with the possibility of substantial H_2O content in the ancient Martian mantle, as revealed by recent assessments of volatile-bearing phases of a meteorite from Mars possibly older than 2.5 Ga [*Agee et al.*, 2013], even the younger shergottites may reflect occasional volatile-rich volcanism during the Amazonian [*Balta and McSween*, 2013]. The discovery of volcanically driven hydrothermal deposits in the Nili Patera caldera [*Skok et al.*, 2010] and Home Plate [*Squyres et al.*, 2008] suggests that hydrothermal activity could have been widespread and long lasting during the perhaps wetter, more volcanically active, Noachian period. Ancient rock strata of Mars also contain phyllosilicates requiring substantial water activity [*Wray et al.*, 2009], and the Noachian surface bears evidence of widespread hydrothermal processes driven by impact activity [*Tornabene et al.*, 2013]. It is possible that a confluence of such factors enabled a high areal density of hydrothermally derived material, incorporated subsequently into bulk soil over geologic time scales, through mechanisms such as deflation and effective aeolian mixing of surface materials. Consequently, we consider hydrothermal activity a possible mechanism to hydrate soil by Fe sulfates on Mars.

Terrestrial analogs also exist for the type of ancient hydrothermal regimes we envision on Mars. For example, low-pH and low water activity hydrothermal regimes (fumaroles) are effective analogs. Occurrence of some Fe hydroxysulfates such as copiapite (Table 1) has been documented at fumaroles [*Yen et al.*, 2008], even though evidence for substantial amounts of hydrous Fe sulfates remains lacking in terrestrial settings [e.g., *Cousins et al.*, 2013]. Also problematic, Fe^{3+} sulfates may predominantly associate with acid mine drainages on Earth. Recent assessments of basaltic pyroclast reactions with sulfuric acid vapor at temperatures above 373 K [*McCollom et al.*, 2013] do not indicate significant quantities of hydrous Fe^{3+} sulfates occurring as a direct alteration product in Martian fumarolic settings. Nevertheless, Fe-sulfate phases may precipitate during evaporation of the associated fluid, particularly at the lower temperature range of hydrothermal environments [e.g., *Tosca and McLennan*, 2006].

A second set of processes, also grounded on the Barnhill Class soil, may reasonably serve as a mechanistic model for the chemical signature of bulk soil: efflorescence. Some hydrous minerals, including Fe sulfates, may effloresce in association with bulk soil moisture variation. Brine films forming within bulk soil may augment this

process, as considered by *Yen et al.* [2008]. However, in many terrestrial settings, effloresced minerals act as cementing mixtures without a dominance of particular groups of minerals [*Joeckel et al.*, 2005]. This may weaken the role of efflorescence as a key mechanism to yield hydrous Fe sulfates from dissolution reactions of Fe sulfide and brines in the subsurface. Nevertheless, efflorescence does deposit minerals such as ferricopiapite, particularly in acid mine drainage environments [*Keith et al.*, 2001]. In the regional context of hydration, as observed in our work, we would consider efflorescence as a secondary mechanism to distribute Fe sulfates, perhaps at scales similar to alteration rinds associated with the loss of sulfur in rocks [*Knoll et al.*, 2008]. Hypothetically, the S lost from rocks to alteration may integrate in the soil component in association with elements such as Fe.

A third process may explain a widespread presence of Fe sulfates in Martian soil, in addition to the two geochemical pathways considered so far. This is the interaction of aerosols and acidic thin water films with finer components of soil over geologic time scales. The volcanic processes discussed previously in this section may have sustained the associated acid fog-type environment at ground level [*Banin et al.*, 1997; *Karunatillake et al.*, 2009]. The associated low water activity would kinetically disfavor the formation of Fe sulfate at detectable concentration at a given location on annual scales, as discussed above for fumarole settings. Nevertheless, prior work by *Golden et al.* [2005] and *Tosca et al.* [2004] demonstrate the potential of acid fog-type reactions to generate many alteration minerals, including Fe sulfates, under Mars analog conditions. Furthermore, prior literature already documents the possibility of regional-scale alteration on Mars driven by acid fog conditions [*McAdam et al.*, 2008; *Karunatillake et al.*, 2009]. Equally important, redox pathways involving hydrous Fe sulfates [*Tosca et al.*, 2008] could also generate chemical signatures of acid fog alteration even without volcanic exhalations. Consequently, over geologic time scales, the low-intensity, yet regionally widespread, acid fog conditions may have contributed to hydrous Fe sulfates in bulk soil.

King and McSween [2005] also considered the possibility that Fe-bearing minerals on Mars may act as signatures of chemical weathering processes over geologic time. The distinct dependence of minerals bearing Fe, H, O, and S on a variety of chemical process variables further motivated their choice of Fe-bearing, often hydrated, sulfates as chemical signatures. These variables include pH, water activity, and bulk composition of the source. *King and McSween* [2005] broadly group the production of the secondary minerals into leaching-dominated (e.g., hydrothermal processes discussed previously in this section) and acid fog-dominated processes.

Since chemical data do not associate directly with detailed mineralogy, we cannot discern which of the two broad process types may contribute dominantly to Martian bulk soil at regional scales. This applies particularly for the sharp contrast in the prediction of few Fe oxides for the acid fog model, compared to many for the leaching model. Nevertheless, predicted chemical signatures [*King and McSween*, 2005] for the leaching model include generally Fe-poor fluids at pH above 4, in contrast to the Fe and sulfate rich fluid of the acid fog model. This tentatively suggests that acid fog processes may yield Fe sulfates more efficiently in Martian soil as secondary minerals. However, the relative dominance of Fe sulfates, compared to other secondary minerals such as phosphates and carbonates associated with cations including Mg and Ca, depends strongly on specific alteration pathways. Furthermore, the leaching and acid fog process predictions do not differ meaningfully in Fe-sulfate abundance at pH below 4 [*King and McSween*, 2005]. Consequently, while our observations are generally consistent with the processes considered throughout this section, we cannot decisively favor the relative contribution of one above the rest.

3.5. Regions of $w(H_2O)$ and $w(S)$ Enrichment and Depletion

Comparisons across bins of enriched H_2O mass fractions, those depleted, and their S counterparts reveal whether the availability of H_2O or of sulfate drives the variation in hydration state. As shown in Figure 6, a clear distinction exists between H_2O enriched and depleted data. Specifically, hydration state distributions, as represented parametrically by their means, differ at nearly three standard deviations. While high S values exist within H_2O enriched areas (red points in Figure 6), considerable overlap with S content in low H_2O regions (orange points in Figure 6) suggests broadly similar S concentration. Consequently, H_2O content alone may cause the variation in hydration state from a low of 2.5 to a high approximating 4.

What might the hydration states across H_2O extrema imply for H_2O chemically bound to sulfates [*Karunatillake et al.*, 2014]? First, the wide range of S content in H_2O enriched regions, evident from the highest S variance among the four regions (Figure 6, red error bar showing standard deviation), supports H_2O association with

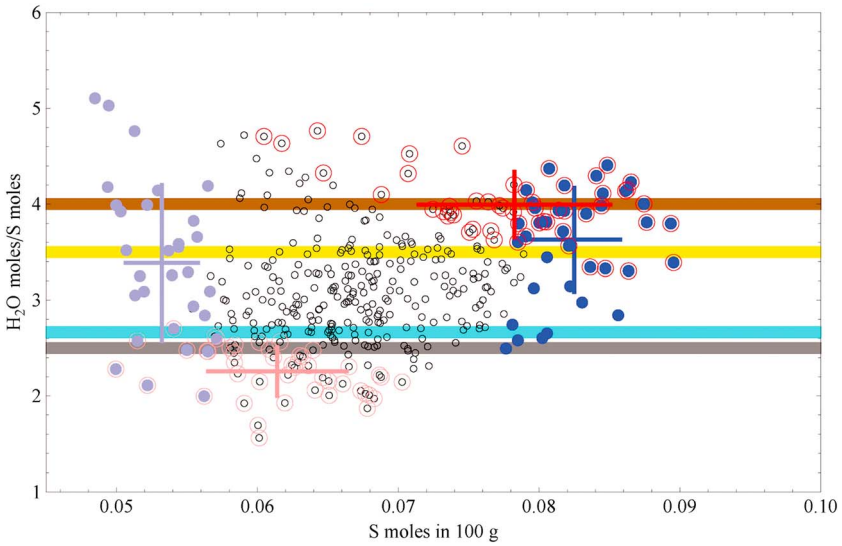

Figure 6. Hydration state versus S moles per 100 g of the subsurface, with regions of H_2O enrichment (red), H_2O depletion (orange), S enrichment (blue), and depletion (green) highlighted. Crosses summarize distributions visually by indicating mean values and standard deviations. While H_2O enriched and depleted regions have distinct hydration states, those of S clearly overlap. Colored bands indicate reference hydration states as in Figure 1. Brown represents starkeyite. Yellow represents ferricopiapite. Coral blue represents kornelite. Gray represents butlerite.

regolith components or processes besides sulfates. Regions of H_2O enrichment also overlap with low thermal inertia regions [e.g., *Gasnault et al*., 2010] common in the north [*Newsom et al*., 2007], where effects such as porosity and grain surface adsorption may dominate due to mantles of fine particles. The significant proportion of low S values within such regions as evident from the highest S variance (Figure 6) indicates that despite some spatial overlap between S and H_2O enriched regions, S bearing phases may not associate consistently with H_2O enriched regolith. By proxy, this also translates into less association of S with fine debris mantles relative to H_2O.

Second, hydration state manifests the least variance within H_2O-depleted regions, along with less S variance than in H_2O enriched regions (Figure 6). This provides additional insight into the association of H_2O with S as a function of H_2O content. The narrower range in S, of mostly lower values, within H_2O-depleted areas supports H_2O chemically bound to sulfates. Minimal variance in hydration state advances this possibility toward specific mineral groups, such as butlerite (Figure 6).

Locations of S enrichment and depletion do not differ considerably in hydration, with both averaging approximately 3.5 (e.g., ferricopiapite), similar to the typical hydration state discussed in section 3.1. Furthermore, hydration states do not head higher in association with S enrichment. Because we quantify hydration state as moles H_2O: moles S, these observations suggest that H_2O varies roughly proportionally with S across S extrema, as expected should H_2O bind to sulfates or to regolith components that contain S. Hydration state comparisons alone cannot distinguish meaningfully among these two and other alternatives that may cause an apparent elemental association.

S extrema do not show hydration state trends that would suggest specific minerals. For example, hydration state variance maximizes in these regions (Figure 6) obscuring any distinction between varying association of H_2O with other regolith components or substantial heterogeneity in hydrous sulfates. While the similar average hydration state across S extrema may reflect H_2O associating chemically with specific sulfate mineral groups, substantiation of the possibility will require complementary mineralogic information, beyond the geochemical focus of this work.

Summarily, hydration state variation within regions of S extrema does not constrain the association of H_2O and S except to suggest the possibility of decoupled H_2O and S distributions. Similar issues exist in H_2O enriched regions. The compelling possibility of H_2O chemically bound to S occurs in H_2O depleted regions, marked by low S variance and the least hydration state variance. By the geographic position in the south,

away from fine debris mantles in the northern hemisphere, these regions also reinforce the possibility of H_2O chemically bound to S in the southern hemisphere [*Karunatillake et al*., 2014].

3.6. Longitudinal and Latitudinal Regression

The observed correlation of H and S, specifically across H and S extrema, could indicate GRS mapping artifacts, analogous to that observed for Fe on the Moon [*Lawrence*, 2002]. Comparing the longitudinal correlations on a quadrangle basis can help us assess this possibility. We divided Mars into 20 "quadrangles" by longitude, with half in the northern hemisphere and half in the southern hemisphere. Consequently, the quadrangles in one hemisphere mirror those in the other, which we compared against one another. The division across the equator allowed each quadrangle to extend 36° longitudinally and to the boundary of mapped data latitudinally. Within these quadrangles, we regressed $10° \times 10°$ binned data for H and S, corresponding approximately to a maximum of 24 data for each regression. The number of data varied by chemical map coverage of the planet, as noted in section 2. In the subsequent discussion, we refer to quadrangles by the R^2 of w(S) regressed with $w(H_2O)$, as shown in Figure 7 (top row).

Figure 7 displays the w(S) of the midlatitudes with the corresponding R^2 value, intercept, and slope of regression with H_2O within each quadrangle. We consider several quadrangles to assess the artifact versus ground truth possibility of γ data. Quadrangles 85 and 91 had the highest range of w(S), as they both contained some of the highest and lowest w(S). In contrast, the longitudinal regions with the smallest range of w(S) (Quadrangles 38 and 64) show smaller R^2. While the quadrangle-based study of w(S) variations across the middle-to-low latitudes demonstrates the influence on regression by the range of w(S), it does not specifically analyze regions of depleted and enriched H and S. Instead, it shows that the scatter in bivariate space gets minimized where the largest dynamic range occurs in both H and S values, yielding the highest correlation (Figure 7). Nevertheless, does evidence for the least scatter and correspondingly highest correlation in quadrangles with the largest dynamic range undermine the case for chemically associated H and S? We think not for four reasons.

First, the dynamic range in H and S remains similar across the hemispheres [*Karunatillake et al*., 2014], but the south shows a high R^2 value despite substantially less scatter. Equally important, the fit residuals in the south range mostly within ±0.5 (Figure 8), comparable to the typical uncertainty per datum of H_2O (0.5) and S (0.1). Since the fit residuals (Figure 8) compare favorably with the uncertainty per datum, we conclude statistically sound regression results relative to the numerical uncertainties of gamma data. Meanwhile, the quadrangles, as regions smaller than the hemispheres by a factor of ~8, show that where the dynamic range maximizes, the correlations become even stronger, predominantly in the southern hemisphere.

Second, we see the smallest dynamic range in the H_2O:S molar ratio in H extrema subsets (depleted set and enriched set) but not in the S extrema subsets (Figure 6, as described in section 3.3). Reduced range in the H_2O:S molar ratio acts as a proxy for stronger correlation, since a less variable ratio indicates that H_2O versus S scatters linearly rather than as a diffuse cloud. This contradicts the expectations from a H_2O:S association driven solely by the dynamic range of both elements. For example, if the H_2O:S associations remained purely a function of dynamic range, the scatter in the H_2O:S ratio should increase in each H extremum because the dynamic range in H gets minimized within. We see a maximized scatter in H_2O:S only in S extrema subsets. Collectively, this suggests that H abundance, not S abundance, underlies the association of H with S. We may consider this geochemically equivalent to not all S phases in the soil binding H, while H binds strongly to available S phases. The positive S intercept in the south, amounting to about 50% of the global S average as shown in our previous work [*Karunatillake et al*., 2014], supports such geochemical possibilities.

Third, if the degree of fine debris mantling acted as the primary source of H-S correlation, the southern hemisphere should show the weakest correlations due to its generally lower dust cover index. On the contrary, we see the strongest correlations in the south, even to the extent of most quadrangles (Figure 7, top, R^2 values are largest in the southern hemisphere). Despite the arbitrary nature of dividing into hemispheres across the equator, the area south of 0° shows meaningfully low mantling relative to the north. On a quadrangle basis, this requires factors other than the degree of mantling to explain locations with the highest dynamic range in both elements. For example, comparing quadrangles 85 and 91, the former shows heavy dust mantling [*Ruff and Christensen*, 2002]. The latter shows mostly low dust mantling.

Fourth, the latitudinal bands do not show compelling evidence for correlation driven primarily by dynamic range. Most latitudinal bands, with 36 data, not only exceed the largest quadrangles by ~50% but also

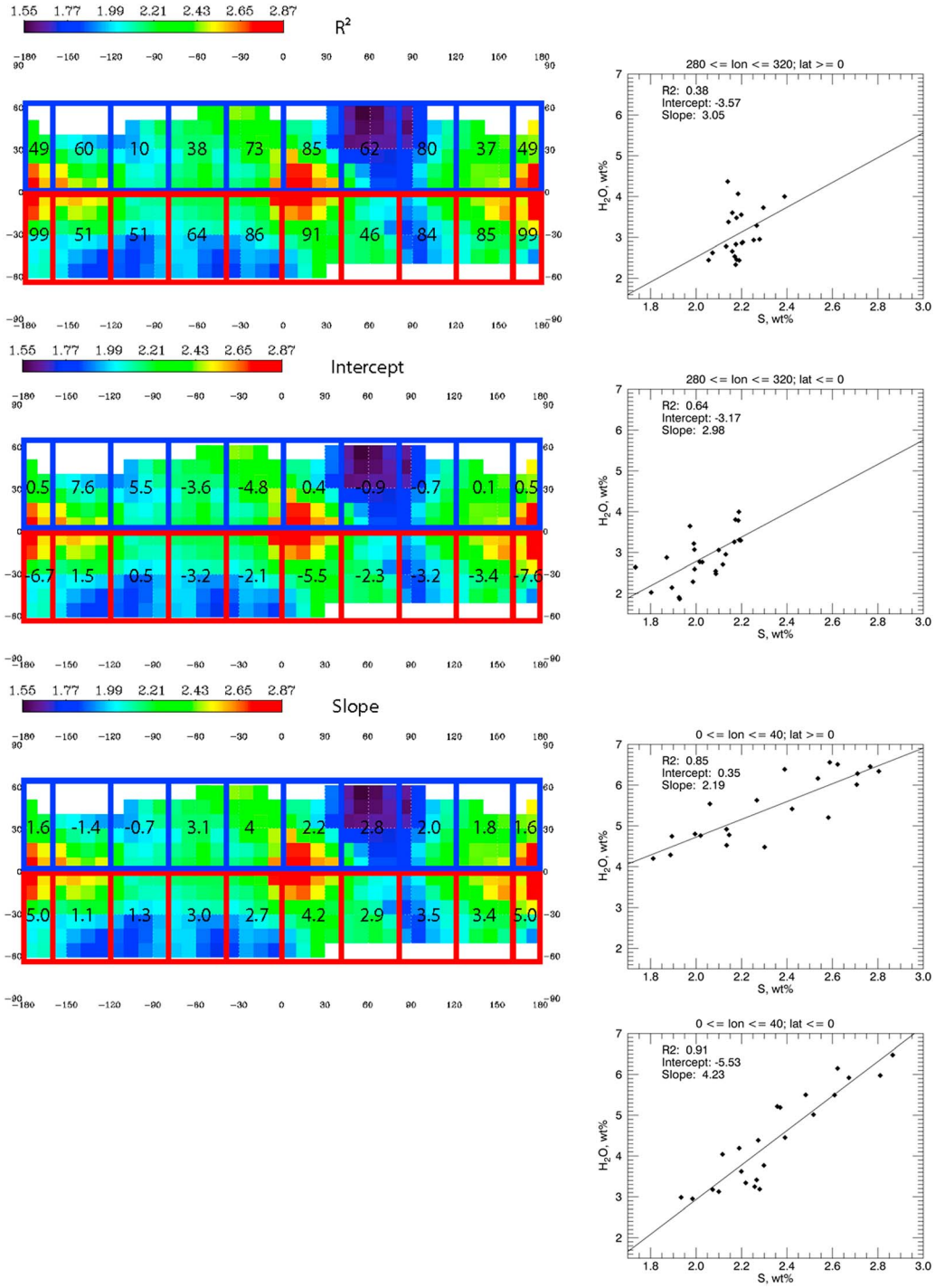

Figure 7. Plot of longitudinal analyses as discussed in section 3.4. *w*(S) distribution in the midlatitudes is indicated by the color scale bar. The upper map is labeled with the coefficient of determination, R^2, as percentage, for *w*(S) and *w*(H_2O) regression in each quadrangle; the middle map lists the regression intercept in each quadrangle, and the bottom map lists the slope in each quadrangle. Quadrangles are named for their R^2 value in the text. Quadrangles 85 and 91 encompass some of the highest and lowest *w*(S) within each, demonstrating the largest range of *w*(S) values within a single quadrangle. Quadrangles 38 and 64 represent the smallest range of *w*(S) values, north and south. We also include four panels as examples among the 18 quadrangles showing how the linear regression parameters reported were obtained. Each panel represents the hydrogen and sulfur abundances measured in 10° × 10° pixels from one quadrangle defined by the longitude/latitude limits given at the top. The intercept, slope, and R^2 of a simple linear regression are calculated and reported.

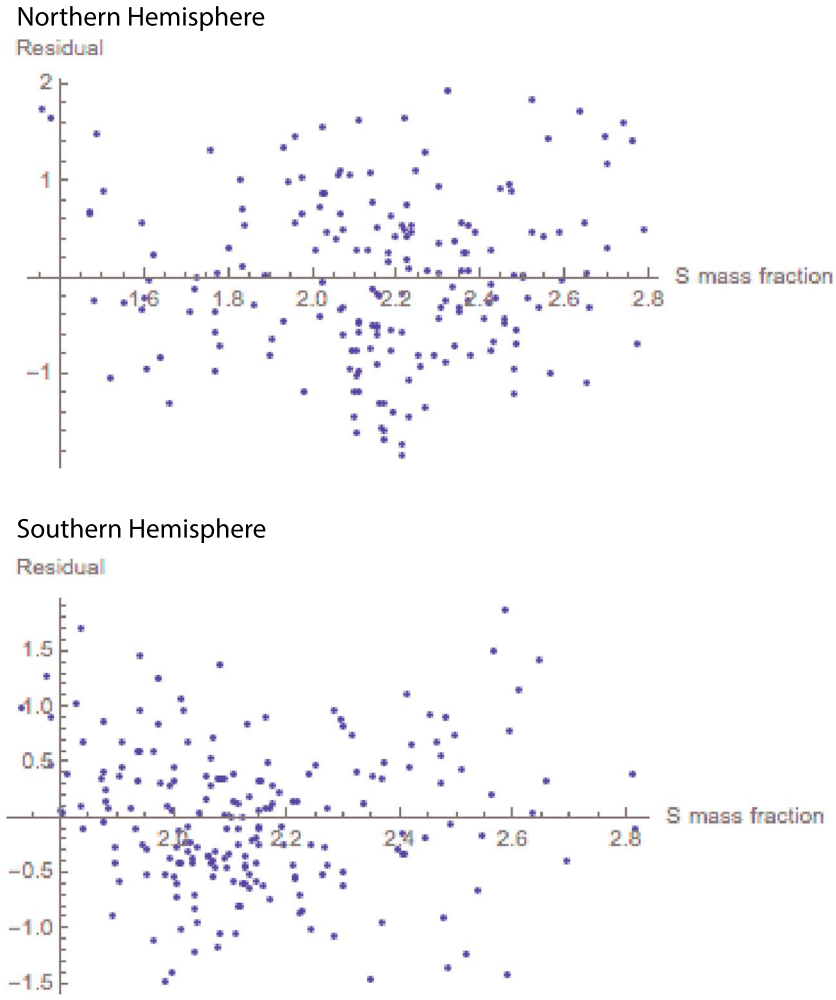

Figure 8. The linear fit residuals for northern and southern hemispheres, plotted against the predictor variable, S, in the regression of H_2O with S mass fractions. Compared to the northern latitudinal band, the southern latitudinal band shows a better fit with residual values typically less than 1.

minimize the impact of spatial autocorrelation by encircling the planet. As an example, we compare the northern latitudinal band centered at 15° (N15) with its southern counterpart (S15) in Figure 9. Both bands show mostly similar dynamic range but 50% lower $R^2 = 0.30$ in N15 relative to S15 ($R^2 = .64$). By sampling a consistently high dynamic range relative to quadrangles, the latitudinal bands effectively show the hemispheric distinctness independent of dynamic range. S25 brings home this point, which preserves an $R^2 = 0.53$ despite a lower dynamic range than N15 in both H and S.

4. Conclusions and Future Work

We attribute the H_2O variation in the southern midlatitudes primarily to sulfates [*Wang et al*., 2013]. In conjunction with the evidence that H_2O availability, not S availability, constrains hydration state (section 3.3 and Figure 6), a spatially variable proportion of a single hydrous mineral group—i.e., Fe sulfates—may underlie our observation. While we cannot exclude mixtures of different hydrous minerals, such mixtures may experience instability over seasonal and diurnal time scales within bulk soil [*Wang and Ling*, 2011].

Terrestrial sulfate mixes of varying hydration are temporally unstable, even though diverse hydration states of adjacent sedimentary rock layers on Mars [*Roach et al*., 2009] may indicate conditions conducive to heterogeneity. Perhaps low temperatures and lithification slow the kinetics [*Berger et al*., 2009] of otherwise thermodynamically unstable mixtures across strata [*Roach et al*., 2009; *Rice et al*., 2011]. However, temporal variability

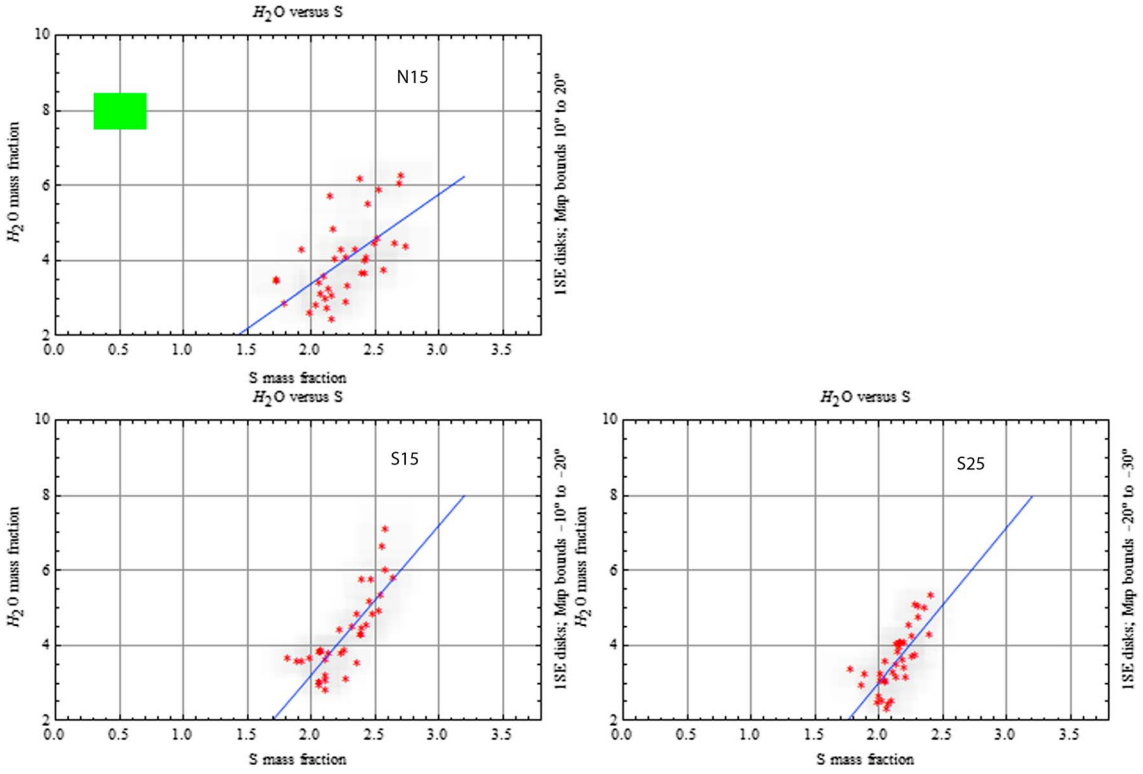

Figure 9. Examples of regressing H_2O with S mass fractions across latitudinal bands. Red dots indicate the data, with the regression line shown in blue. To prevent clutter, the green rectangle shows the typical uncertainty of H_2O and S mass fractions globally, computed as the root-mean-square value. Latitudinal bands are identified along the right *y* axis of each graph and the center latitude by N15, S15, and S25.

of exposed subsurface soil spectra at Gusev Crater reveals that some sulfate mixtures destabilize upon exposure to a humidity gradient [*Wang and Ling*, 2011]. Exact physicochemical pathways that stabilize heterogenous hydration states, particularly of anhydrous and hydrous sulfates comingled at instrumental spatial resolutions, remain to be understood. Simulations under Martian conditions of Fe-sulfate mixtures following on the work by *Xu et al.* [2010], *Rice et al.* [2011], *Wang et al.* [2006, 2008, 2013], and *Wang and Ling* [2011] may prove helpful in this regard.

The latitudinal variation in hydration states provides detailed insight into compositional variation in the southern hemisphere where hydration states may reflect chemical composition more accurately than in the north. Our observations of the H_2O-enriched regions, located predominantly in the northern hemispheric areas of fine debris mantles, suggest a major role to nonsulfate phases driving the distribution of H_2O. Atmospheric conditions that produced the northern dust mantles [*Newsom et al.*, 2007] may have contributed with $H_2O(s)$ [*Eastwood et al.*, 2008; *Niles and Michalski*, 2009] nucleating on fine grains, causing an increased H_2O budget for sulfate hydration. This is consistent with our evidence that H_2O, not sulfates, drives the hydration.

Contrasting with the north, latitudinal variations in the southern highlands, as described in section 3.2 and Figure 5, supports Fe sulfate as a primary hydration mineral in bulk soil [*Lane et al.*, 2004]. Minor proportions of Ca and Mg sulfates appear limited to a few latitudinal bands, particularly 10°–20°S, as evident in synoptic Figure 5 and related text (section 3.2). The likely areal and depth pervasiveness of hydrous Fe sulfates as the mode of bulk soil hydration reinforces the importance of investigating genetic processes of Paso Robles-type soil at Gusev Crater, including the possibility that this type soil may represent a component of Martian bulk soil in the southern hemisphere.

Among the several genetic processes considered by *Yen et al.* [2008] for Paso Robles type soil, one seems applicable at regional scales: hydrothermal deposits deflated and integrated into bulk soil regionally. Icelandic terrestrial analogs of the putative Nili Patera hydrothermal deposit [*Skok et al.*, 2010] may provide critical constraints by revealing whether hydrous Fe sulfates may exist as a key mineralogic component in

such environments [*Cousins et al*., 2013]. This may alter or reinforce the impression discussed in section 3.2 that terrestrial hydrothermal environments do not yield hydrous Fe sulfates at high mass fractions [e.g., *Cousins et al*., 2013]. Equally important for future work, the discovery of hydrothermal deposits of intact geologic context at Nili Patera [*Skok et al*., 2010] and of relatively eroded deposits at Gusev Crater of obscure provenance [e.g., *Lewis et al*., 2008; *Squyres et al*., 2008] enable a preliminary framework for deflation rates in Martian hydrothermal deposits. Estimated deflation rates will help to determine the feasibility of hydrothermal products contributing to bulk soil at regional scale. Fleeting yet geologically frequent impact hydrothermal environments [e.g., *Tornabene et al*., 2013] may also contribute meaningfully to bulk soil, with our study motivating a closer assessment of Fe-bearing mineral phases in Martian impact environments. This may apply particularly in the southern hemisphere's relatively ancient terrain.

The GRS provides regional, global, and depth context to sulfates detected locally with VNTIR in orbit and in situ by rovers and landers. The global distribution of hydration states in the southern midlatitudes supports Fe sulfates as a primary H_2O carrier among them, perhaps analogous to Paso Robles-type soil at Gusev Crater. Minerals such as kieserite, epsomite, and hexahydrite, which appear pervasive in localities including Valles Marineris as observed by VNTIR, do not appear to dominate the subsurface composition. This may be driven by compositional layering deeper than the hundreds of micron depths sampled by VNTIR observations, by different minerals dominating at regional scales than local scales, or a combination of both. However, we cannot exclude mixtures of minimally and maximally hydrous Mg and Ca sulfates, which could be variable at depth and at regional spatial scales. Regardless, hydrous Fe sulfates could be a key component hydrating Martian bulk soil [*Lane et al*., 2004], especially in the southern hemisphere.

Acknowledgments
We thank Steven A. Hauck, the Editor-in-Chief at JGR-Planets as well as the reviewer Melissan Lane whose thoughtful critique enables us to make major improvements to the manuscript. We also thank the anonymous reviewers. We make the data available via NASA's PDS. We thank Dave Hamara and the Mars Odyssey GRS team for collegial support. This research of the Mars Odyssey project was supported by NASA/Jet Propulsion Lab and by NASA Mars Data Analysis Program grants NNX07AN96G and NNX10AQ23G to Scott McLennan. MDAP grants NNX12AG89G and NNX13AI98G provided funding to the Planetary Science Lab led by Suniti Karunatillake. LSU's College of Science and Geology and Geophysics provided postdoctoral fellowship support to J.R. Skok.

References

Ackiss, S. E., and J. J. Wray (2014), Occurrences of possible hydrated sulfates in the southern high latitudes of Mars, *Icarus*, *243*, 311–324, doi:10.1016/j.icarus.2014.08.016.

Agee, C. B., et al. (2013), Unique meteorite from early Amazonian Mars: Water-rich basaltic breccia Northwest Africa 7034, *Science*, *339*(6121), 780–785, doi:10.1126/science.1228858.

Archer, P. D., et al. (2014), Abundances and implications of volatile-bearing species from evolved gas analysis of the Rocknest aeolian deposit, Gale Crater, Mars, *J. Geophys. Res. Planets*, *119*, 237–254, doi:10.1002/2013JE004493.

Balta, J. B., and H. Y. McSween (2013), Water and the composition of Martian magmas, *Geology*, *41*(10), 1115–1118, doi:10.1130/G34714.1.

Banin, A., et al. (1997), Acidic volatiles and the Mars Soil, *J. Geophys. Res.*, *102*, 13,341–13,356, doi:10.1029/97JE01160.

Beck, P., A. Pommerol, B. Schmitt, and O. Brissaud (2010), Kinetics of water adsorption on minerals and the breathing of the Martian regolith, *J. Geophys. Res.*, *115*, E10011, doi:10.1029/2009JE003539.

Berger, G., M. J. Toplis, E. Treguier, C. d'Uston, and P. Pinet (2009), Evidence in favor of small amounts of ephemeral and transient water during alteration at Meridiani Planum, Mars, *Am. Mineral.*, *94*(8-9), 1279–1282, doi:10.2138/am.2009.3230.

Bishop, J. L., et al. (2009), Mineralogy of Juventae Chasma: Sulfates in the light-toned mounds, mafic minerals in the bedrock, and hydrated silica and hydroxylated ferric sulfate on the plateau, *J. Geophys. Res.*, *114*, E00D09, doi:10.1029/2009JE003352.

Bishop, J. L., D. Loizeau, N. K. McKeown, L. Saper, M. D. Dyar, D. J. Des Marais, M. Parente, and S. L. Murchie (2013), What the ancient phyllosilicates at Mawrth Vallis can tell us about possible habitability on early Mars, *Planet. Space Sci.*, *86*, 130–149, doi:10.1016/j.pss.2013.05.006.

Bouezmarni, T., and O. Scaillet (2005), Consistency of asymmetric kernel density estimators and smoothed histograms with application to income data, *Econom. Theory*, *21*, 390–412, doi:10.1017/S0266466605050218.

Boynton, W. V., et al. (2007), Concentration of H, Si, Cl, K, Fe, and Th in the low- and mid-latitude regions of Mars, *J. Geophys. Res.*, *112*, E12S99, doi:10.1029/2007JE002887.

Bridges, N., F. Ayoub, J.-P. Avouac, S. Leprince, A. Lucas, and S. S. Mattson (2012), Earth-like sand fluxes on Mars, *Nature*, *485*(7398), 339–342, doi:10.1038/nature11022.

Byrne, S., et al. (2009), Distribution of mid-latitude ground ice on Mars from new impact craters, *Science*, *325*(5948), 1674–1676, doi:10.1126/science.1175307.

Certini, G., and F. C. Ugolini (2013), An updated, expanded, universal definition of soil, *Geoderma*, *192*, 378–379, doi:10.1016/j.geoderma.2012.07.008.

Christensen, P. R., et al. (2004), The Thermal Emission Imaging System (THEMIS) for the Mars 2001 Odyssey Mission, *Space Sci. Rev.*, *110*, 85–130, doi:10.1023/B:SPAC.0000021008.16305.94.

Clark, B. C., et al. (2005), Chemistry and mineralogy of outcrops at Meridiani Planum, *Earth Planet. Sci. Lett.*, *240*(1), 73–94, doi:10.1016/j.epsl.2005.09.040.

Cloutis, E. A., et al. (2006), Detection and discrimination of sulfate minerals using reflectance spectroscopy, *Icarus*, *184*, 121–157, doi:10.1016/j.icarus.2006.04.003.

Cousins, C. R., et al. (2013), Glaciovolcanic hydrothermal environments in Iceland and implications for their detection on Mars, *J. Volcanol. Geotherm. Res.*, *256*, 61–77, doi:10.1016/j.jvolgeores.2013.02.009.

Diez, B., W. C. Feldman, N. Mangold, D. Baratoux, S. Maurice, O. Gasnault, L. D'Uston, and F. Costard (2009), Contribution of Mars Odyssey GRS at central Elysium Planitia, *Icarus*, *200*(1), 19–29, doi:10.1016/j.icarus.2008.11.011.

Eastwood, M. L., S. Cremel, C. Gehrke, E. Girard, and A. K. Bertram (2008), Ice nucleation on mineral dust particles: Onset conditions, nucleation rates and contact angles, *J. Geophys. Res.*, *113*, D22203, doi:10.1029/2008JD010639.

Ehlmann, B. L., et al. (2009), Identification of hydrated silicate minerals on Mars using MRO-CRISM: Geologic context near Nili Fossae and implications for aqueous alteration, *J. Geophys. Res.*, *114*, E00D08, doi:10.1029/2009JE003339.

Elgammal, A., R. Duraiswami, D. Harwood, and L. S. Davis (2002), Background and foreground modeling using nonparametric kernel density estimation for visual surveillance, *Proc. IEEE*, *90*(7), 1151–1163, doi:10.1109/JPROC.2002.801448.

Farquhar, J., J. Savarino, T. L. Jackson, and M. H. Thiemens (2000), Evidence of atmospheric sulphur in the Martian regolith from sulphur isotopes in meteorites, *Nature*, *404*(6773), 50–52, doi:10.1038/35003517.

Fedo, C. M., I. O. McGlynn, and H. Y. McSween Jr. (2015), Grain size and hydrodynamic sorting controls on the composition of basaltic sediments: Implications for interpreting Martian soils, *Earth Planet. Sci. Lett.*, *423*, 67–77, doi:10.1016/j.epsl.2015.03.052.

Feldman, W. C., et al. (2004), Hydrated states of $MgSO_4$ at equatorial latitudes on Mars, *Geophys. Res. Lett.*, *31*, L16702, doi:10.1029/2004GL020181.

Feldman, W. C., et al. (2005), Topographic control of hydrogen deposits at low latitudes to midlatitudes of Mars, *J. Geophys. Res.*, *110*, E11009, doi:10.1029/2005JE002452.

Gasnault, O., G. Jeffrey Taylor, S. Karunatillake, J. M. Dohm, H. E. Newsom, O. Forni, P. Pinet, and W. V. Boynton (2010), Quantitative geochemical mapping of Martian elemental provinces, *Icarus*, *207*(1), 226–247, doi:10.1016/j.icarus.2009.11.010.

Gendrin, A., et al. (2005), Sulfates in Martian layered terrains: The OMEGA/Mars Express view, *Science*, *307*(5715), 1587–1591, doi:10.1126/science.1109087.

Glavin, D. P., et al. (2013), Evidence for perchlorates and the origin of chlorinated hydrocarbons detected by SAM at the Rocknest aeolian deposit in Gale Crater, *J. Geophys. Res. Planets*, *118*, 1955–1973, doi:10.1002/jgre.20144.

Golden, D. C., D. W. Ming, R. V. Morris, and S. A. Mertzman (2005), Laboratory-simulated acid-sulfate weathering of basaltic materials: Implications for formation of sulfates at Meridiani Planum and Gusev crater, Mars, *J. Geophys. Res.*, *110*, E12S07, doi:10.1029/2005JE002451.

Halevy, I., and D. P. Schrag (2009), Sulfur dioxide inhibits calcium carbonate precipitation: Implications for early Mars and Earth, *Geophys. Res. Lett.*, *36*, L23201, doi:10.1029/2009GL040792.

Halevy, I., M. T. Zuber, and D. P. Schrag (2007), A sulfur dioxide climate feedback on early Mars, *Science*, *318*(5858), 1903–1907, doi:10.1126/science.1147039.

Hamrick, J. (2008), Kernel density estimation, Wolfram Demonstr. Proj. [Available at http://demonstrations.wolfram.com/KernelDensityEstimation/.]

Haskin, L. A., et al. (2005), Water alteration of rocks and soils on Mars at the Spirit rover site in Gusev crater, *Nature*, *436*(7047), 66–69, doi:10.1038/nature03640.

Hecht, M. H., et al. (2009), Detection of perchlorate and the soluble chemistry of Martian soil at the Phoenix lander site, *Science*, *325*(5936), 64–67, doi:10.1126/science.1172466.

Jakosky, B. M., M. T. Mellon, E. Varnes, W. C. Feldman, W. V. Boynton, and R. Haberle (2005), Mars low-latitude neutron distribution: Possible remnant near-surface water ice and a mechanism for its recent emplacement, *Icarus*, *175*(1), 58–67, doi:10.1016/j.icarus.2004.11.014.

Jänchen, J., R. V. Morris, D. L. Bish, M. Janssen, and U. Hellwig (2009), The H_2O and CO_2 adsorption properties of phyllosilicate-poor palagonitic dust and smectites under Martian environmental conditions, *Icarus*, *200*(2), 463–467, doi:10.1016/j.icarus.2008.12.006.

Joeckel, R. M., B. J. Ang Clement, and L. R. VanFleet Bates (2005), Sulfate-mineral crusts from pyrite weathering and acid rock drainage in the Dakota Formation and Graneros Shale, Jefferson County, Nebraska, *Chem. Geol.*, *215*(1–4), 433–452, doi:10.1016/j.chemgeo.2004.06.044.

Johnson, J. R., J. F. Bell III, E. Cloutis, M. Staid, W. H. Farrand, T. McCoy, M. Rice, A. Wang, and A. Yen (2007), Mineralogic constraints on sulfur-rich soils from Pancam spectra at Gusev crater, Mars, *Geophys. Res. Lett.*, *34*, L13202, doi:10.1029/2007GL029894.

Jouglet, D., F. Poulet, R. E. Milliken, J. F. Mustard, J.-P. Bibring, Y. Langevin, B. Gondet, and C. Gomez (2007), Hydration state of the Martian surface as seen by Mars Express OMEGA: 1. Analysis of the 3 μm hydration feature, *J. Geophys. Res.*, *112*, E08S06, doi:10.1029/2006JE002846.

Karunatillake, S., J. M. Keller, S. W. Squyres, W. V. Boynton, J. Brückner, D. M. Janes, O. Gasnault, and H. E. Newsom (2007), Chemical compositions at Mars landing sites subject to Mars Odyssey Gamma Ray Spectrometer constraints, *J. Geophys. Res.*, *112*, E08S90, doi:10.1029/2006JE002859.

Karunatillake, S., J. J. Wray, S. W. Squyres, G. J. Taylor, O. Gasnault, S. M. McLennan, W. V. Boynton, M. R. El Maarry, and J. M. Dohm (2009), Chemically striking regions on Mars and Stealth revisited, *J. Geophys. Res.*, *114*, E12001, doi:10.1029/2008JE003303.

Karunatillake, S., S. W. Squyres, O. Gasnault, J. M. Keller, D. M. Janes, W. V. Boynton, and M. J. Finch (2010), Recipes for spatial statistics with global datasets: A Martian case study, *J. Sci. Comput.*, *46*(3), 439–451, doi:10.1007/s10915-010-9412-z.

Karunatillake, S., O. Gasnault, S. W. Squyres, J. M. Keller, D. M. Janes, W. V. Boynton, and H. E. Newsom (2012), Martian case study of multivariate correlation and regression with planetary datasets, *Earth Moon Planets*, *108*, 253–273, doi:10.1007/s11038-012-9395-x.

Karunatillake, S., J. J. Wray, O. Gasnault, S. M. McLennan, A. D. Rogers, S. W. Squyres, W. V. Boynton, J. R. Skok, L. Ojha, and N. Olsen (2014), Sulfates hydrating bulk soil in the Martian low and middle latitudes, *Geophys. Res. Lett.*, *41*, 7987–7996, doi:10.1002/2014GL061136.

Keith, D. C., D. D. Runnells, K. J. Esposito, J. A. Chermak, D. B. Levy, S. R. Hannula, M. Watts, and L. Hall (2001), Geochemical models of the impact of acidic groundwater and evaporative sulfate salts on Boulder Creek at Iron Mountain, California, *Appl. Geochemistry*, *16*(7-8), 947–961, doi:10.1016/S0883-2927(00)00080-9.

King, P. L., and H. Y. McSween (2005), Effects of H_2O, pH, and oxidation state on the stability of Fe minerals on Mars, *J. Geophys. Res.*, *110*, E12S10, doi:10.1029/2005JE002482.

King, P. L., and S. M. McLennan (2010), Sulfur on Mars, *Elements*, *6*(2), 107–112, doi:10.2113/gselements.6.2.107.

Knoll, A. H., et al. (2008), Veneers, rinds, and fracture fills: Relatively late alteration of sedimentary rocks at Meridiani Planum, Mars, *J. Geophys. Res.*, *113*, E06S16, doi:10.1029/2007JE002949.

Lane, M. D., M. D. Dyar, and J. L. Bishop (2004), Spectroscopic evidence for hydrous iron sulfate in the Martian soil, *Geophys. Res. Lett.*, *31*, L19702, doi:10.1029/2004GL021231.

Lane, M. D., J. L. Bishop, M. Darby Dyar, P. L. King, M. Parente, and B. C. Hyde (2008), Mineralogy of the Paso Robles soils on Mars, *Am. Mineral.*, *93*(5-6), 728–739, doi:10.2138/am.2008.2757.

Lane, M. D., J. L. Bishop, M. D. Dyar, T. Hiroi, S. A. Mertzman, D. L. Bish, P. L. King, and A. D. Rogers (2015), Mid-infrared emission spectroscopy and visible/near-infrared reflectance spectroscopy of Fe-sulfate minerals, *Am. Mineral.*, *100*, 66–82, doi:10.2138/am.2014.4762.

Lawrence, D. J. (2002), Iron abundances on the lunar surface as measured by the Lunar Prospector gamma-ray and neutron spectrometers, *J. Geophys. Res.*, *107*(E12), 5130, doi:10.1029/2001JE001530.

Lewis, K. W., O. Aharonson, J. P. Grotzinger, S. W. Squyres, J. F. Bell III, L. S. Crumpler, and M. E. Schmidt (2008), Structure and stratigraphy of Home Plate from the Spirit Mars Exploration Rover, *J. Geophys. Res.*, *113*, E12S36, doi:10.1029/2007JE003025.

Liu, X., Q. Song, and P. Li (2009), A parabolic detection algorithm based on kernel density estimation, in *Emerging Intelligent Computing Technology and Applications*, edited by D.-S. Huang et al., pp. 405–412, Springer, Berlin.

McAdam, A. C., M. Y. Zolotov, T. G. Sharp, and L. A. Leshin (2008), Preferential low-pH dissolution of pyroxene in plagioclase-pyroxene mixtures: Implications for Martian surface materials, *Icarus*, *196*, 90–96, doi:10.1016/j.icarus.2008.01.008.

McAdam, A. C., et al. (2014), Sulfur-bearing phases detected by evolved gas analysis of the Rocknest aeolian deposit, Gale Crater, Mars, *J. Geophys. Res. Planets*, *119*, 373–393, doi:10.1002/2013JE004518.
McCollom, T. M., M. Robbins, B. Moskowitz, T. S. Berquó, N. Jöns, and B. M. Hynek (2013), Experimental study of acid-sulfate alteration of basalt and implications for sulfate deposits on Mars, *J. Geophys. Res. Planets*, *118*, 577–614, doi:10.1002/jgre.20044.
McEwen, A. S., L. Ojha, C. M. Dundas, S. S. Mattson, S. Byrne, J. J. Wray, S. C. Cull, S. L. Murchie, N. Thomas, and V. C. Gulick (2011), Seasonal flows on warm Martian slopes, *Science*, *333*(6043), 740–743, doi:10.1126/science.1204816.
McEwen, A. S., C. M. Dundas, S. S. Mattson, A. D. Toigo, L. Ojha, J. J. Wray, M. Chojnacki, S. Byrne, S. L. Murchie, and N. Thomas (2014), Recurring slope lineae in equatorial regions, *Nat. Geosci.*, *7*, 53–58, doi:10.1038/NGEO2014.
McGlynn, I. O., C. M. Fedo, and H. Y. McSween (2011), Origin of basaltic soils at Gusev crater, Mars, by aeolian modification of impact-generated sediment, *J. Geophys. Res.*, *116*, E00F22, doi:10.1029/2010JE003712.
McSween, H. Y., I. O. McGlynn, and A. D. Rogers (2010), Determining the modal mineralogy of Martian soils, *J. Geophys. Res.*, *115*, E00F12, doi:10.1029/2010JE003582.
Meslin, P., et al. (2013), Soil Diversity and hydration as observed by ChemCam at Gale crater, Mars, *Science*, *341*, 1–10.
Michalski, J. R., J. Cuadros, P. B. Niles, J. Parnell, A. D. Rogers, and S. P. Wright (2013), Groundwater activity on Mars and implications for a deep biosphere, *Nat. Geosci.*, *6*(2), 133–138, doi:10.1038/ngeo1706.
Milliken, R. E., J. F. Mustard, F. Poulet, D. Jouglet, J.-P. Bibring, B. Gondet, and Y. Langevin (2007), Hydration state of the Martian surface as seen by Mars Express OMEGA: 2. H_2O content of the surface, *J. Geophys. Res.*, *112*, E08S07, doi:10.1029/2006JE002853.
Morris, R. V., et al. (2006), Mössbauer mineralogy of rock, soil, and dust at Gusev crater, Mars: Spirit's journey through weakly altered olivine basalt on the plains and pervasively altered basalt in the Columbia Hills, *J. Geophys. Res.*, *111*, E02S13, doi:10.1029/2005JE002584.
Morris, R. V., D. C. Golden, D. W. Ming, T. G. Graff, R. E. Arvidson, S. M. Wiseman, K. A. Lichtenberg, and S. Cull (2009), Visible and near-IR reflectance spectra for smectite, sulfate and perchlorate under dry conditions for interpretation of Martian surface mineralogy, in *40th Lunar and Planetary Science Conference*, Abstract 2317, Lunar and Planetary Institute, Houston, Tex.
Murchie, S. L., et al. (2009), A synthesis of Martian aqueous mineralogy after 1 Mars year of observations from the Mars Reconnaissance Orbiter, *J. Geophys. Res.*, *114*, E00D06, doi:10.1029/2009JE003342.
Navarro- González, R., E. Vargas, J. de la Rosa, A. C. Raga, and C. P. Mckay (2010), Reanalysis of the Viking results suggests perchlorate and organics at midlatitudes on Mars, *J. Geophys. Res.*, *115*, E12010, doi:10.1029/2010JE003599.
Newsom, H. E., et al. (2007), Geochemistry of Martian soil and bedrock in mantled and less mantled terrains with gamma ray data from Mars Odyssey, *J. Geophys. Res.*, *112*, E03S12, doi:10.1029/2006JE002680.
Niles, P. B., and J. R. Michalski (2009), Meridiani Planum sediments on Mars formed through weathering in massive ice deposits, *Nat. Geosci.*, *2*(3), 215–220, doi:10.1038/ngeo438.
Noe Dobrea, E. Z., et al. (2010), Mineralogy and stratigraphy of phyllosilicate-bearing and dark mantling units in the greater Mawrth Vallis/west Arabia Terra area: Constraints on geological origin, *J. Geophys. Res.*, *115*, E00D19, doi:10.1029/2009JE003351.
Ojha, L., M. B. Wilhelm, S. L. Murchie, A. S. McEwen, J. J. Wray, J. Hanley, M. Massé, and M. Chojnacki (2015), Spectral evidence for hydrated salts in recurring slope lineae on Mars, *Nat. Geosci.*, *8*(11), 829–832, doi:10.1038/ngeo2546.
Peng, Y., H. Bao, L. M. Pratt, A. J. Kaufman, G. Jiang, C. Zhou, and X. Yuan (2014), Widespread contamination of carbonate-associated sulfate by present-day secondary atmospheric sulfate: Evidence from triple oxygen isotopes, *Geology*, *42*(9), 815–818, doi:10.1130/G35852.1.
Pitman, K. M., E. Z. Noe Dobrea, C. S. Jamieson, J. B. Dalton III, W. J. Abbey, and E. C. S. Joseph (2014), Reflectance spectroscopy and optical functions for hydrated Fe-sulfates, *Am. Mineral.*, *99*, 1593–1603, doi:10.2138/am.2014.4730.
Poulet, F., C. Gomez, J.-P. Bibring, Y. Langevin, B. Gondet, P. Pinet, G. Belluci, and J. F. Mustard (2007), Martian surface mineralogy from Observatoire pour la Minéralogie, l'Eau, les Glaces et l'Activité on board the Mars Express spacecraft (OMEGA/MEx): Global mineral maps, *J. Geophys. Res.*, *112*, E08S02, doi:10.1029/2006JE002840.
Rice, M. S., J. F. Bell III, E. A. Cloutis, J. J. Wray, K. E. Herkenhoff, R. Sullivan, J. R. Johnson, and R. B. Anderson (2011), Temporal observations of bright soil exposures at Gusev crater, Mars, *J. Geophys. Res.*, *116*, E00F14, doi:10.1029/2010JE003683.
Righter, K., K. Pando, and L. R. Danielson (2009), Experimental evidence for sulfur-rich Martian magmas: Implications for volcanism and surficial sulfur sources, *Earth Planet. Sci. Lett.*, *288*(1–2), 235–243, doi:10.1016/j.epsl.2009.09.027.
Roach, L. H., J. F. Mustard, S. L. Murchie, J.-P. Bibring, F. Forget, K. W. Lewis, O. Aharonson, M. Vincendon, and J. L. Bishop (2009), Testing evidence of recent hydration state change in sulfates on Mars, *J. Geophys. Res.*, *114*, E00D02, doi:10.1029/2008JE003245.
Ruff, S. W., and P. R. Christensen (2002), Bright and dark regions on Mars: Particle size and mineralogical characteristics based on Thermal Emission Spectrometer data, *J. Geophys. Res.*, *107*(E12), 5127, doi:10.1029/2001JE001580.
Schröder, S., P.-Y. Meslin, A. Cousin, O. Gasnault, W. Rapin, J. Blank, J. Lasue, S. Maurice, R. C. Wiens, and M. S. L. Science Team (2014), ChemCam hydrogen detection in soils and dust along Curiosity's traverse, in *8th International Conference on Mars*, Abstract 1214, Lunar Planet. Inst., Pasadena, Calif.
Sheather, S. J., and M. C. Jones (1991), A reliable data-based bandwidth selection method for kernel density estimation, *J. R. Stat. Soc. Ser. B*, *53*(3), 683–690.
Shimazaki, H., and S. Shinomoto (2010), Kernel bandwidth optimization in spike rate estimation, *J. Comput. Neurosci.*, *29*(1–2), 171–182, doi:10.1007/s10827-009-0180-4.
Sklute, E. C., H. B. Jensen, A. D. Rogers, and R. J. Reeder (2015), Morphological, structural, and spectral characteristics of amorphous iron sulfates, *J. Geophys. Res. Planets*, *120*, 809–830, doi:10.1002/2014JE004784.
Skok, J. R., J. F. Mustard, B. L. Ehlmann, R. E. Milliken, and S. L. Murchie (2010), Silica deposits in the Nili Patera caldera on the Syrtis Major volcanic complex on Mars, *Nat. Geosci.*, *3*(12), 838–841, doi:10.1038/ngeo990.
Squyres, S. W., and L. G. Evans (1992), Effects of material mixing on planetary gamma ray spectroscopy, *J. Geophys. Res.*, *97*, 14,701–14,715, doi:10.1029/92JE01671.
Squyres, S. W., et al. (2008), Detection of silica-rich deposits on Mars, *Science*, *320*(5879), 1063–1067, doi:10.1126/science.1155429.
Steiger, M., K. Linnow, D. Ehrhardt, and M. Rohde (2011), Decomposition reactions of magnesium sulfate hydrates and phase equilibria in the $MgSO_4$–H_2O and Na^+–Mg^{2+}–Cl^-–SO_4^{2-}–H_2O systems with implications for Mars, *Geochim. Cosmochim. Acta*, *75*(12), 3600–3626, doi:10.1016/j.gca.2011.03.038.
Szynkiewicz, A., D. M. Borrok, and D. T. Vaniman (2014), Efflorescence as a source of hydrated sulfate minerals in valley settings on Mars, *Earth Planet. Sci. Lett.*, *393*, 14–25, doi:10.1016/j.epsl.2014.02.035.
Taylor, G. J., L. M. V. Martel, S. Karunatillake, O. Gasnault, and W. V. Boynton (2010), Mapping Mars geochemically, *Geology*, *38*(2), 183–186, doi:10.1130/G30470.1.

Tornabene, L. L., G. R. Osinski, A. S. McEwen, J. J. Wray, M. A. Craig, H. M. Sapers, and P. R. Christensen (2013), An impact origin for hydrated silicates on Mars: A synthesis, *J. Geophys. Res. Planets*, *118*, 994–1012, doi:10.1002/jgre.20082.

Tosca, N. J., and S. M. McLennan (2006), Chemical divides and evaporite assemblages on Mars, *Earth Planet. Sci. Lett.*, *241*(1-2), 21–31, doi:10.1016/j.epsl.2005.10.021.

Tosca, N. J., S. M. McLennan, D. H. Lindsley, and M. A. A. Schoonen (2004), Acid-sulfate weathering of synthetic Martian basalt: The acid fog model revisited, *J. Geophys. Res.*, *109*, E05003, doi:10.1029/2003JE002218.

Tosca, N. J., A. H. Knoll, and S. M. McLennan (2008), Water activity and the challenge for life on early Mars, *Science*, *320*(5880), 1204–1207, doi:10.1126/science.1155432.

Wang, A., and Z. Ling (2011), Ferric sulfates on Mars: A combined mission data analysis of salty soils at Gusev crater and laboratory experimental investigations, *J. Geophys. Res.*, *116*, E00F17, doi:10.1029/2010JE003665.

Wang, A., J. J. Freeman, B. L. Jolliff, and I.-M. Chou (2006), Sulfates on Mars: A systematic Raman spectroscopic study of hydration states of magnesium sulfates, *Geochim. Cosmochim. Acta*, *70*(24), 6118–6135, doi:10.1016/j.gca.2006.05.022.

Wang, A., et al. (2008), Light-toned salty soils and coexisting Si-rich species discovered by the Mars Exploration Rover Spirit in Columbia Hills, *J. Geophys. Res.*, *113*, E12S40, doi:10.1029/2008JE003126.

Wang, A., J. J. Freeman, and B. L. Jolliff (2009), Phase transition pathways of the hydrates of magnesium sulfate in the temperature range 50 °C to 5 °C: Implication for sulfates on Mars, *J. Geophys. Res.*, *114*, E04010, doi:10.1029/2008JE003266.

Wang, A., W. C. Feldman, M. T. Mellon, and M. Zheng (2013), The preservation of subsurface sulfates with mid-to-high degree of hydration in equatorial regions on Mars, *Icarus*, *226*, 980–991, doi:10.1016/j.icarus.2013.07.020.

Wieser, M. E. (2006), Atomic weights of the elements 2005 (IUPAC Technical Report), *Pure Appl. Chem.*, *78*(11), 2051–2066, doi:10.1351/pac200678112051.

Wray, J. J., S. L. Murchie, S. W. Squyres, F. P. Seelos, and L. L. Tornabene (2009), Diverse aqueous environments on ancient Mars revealed in the southern highlands, *Geology*, *37*(11), 1043–1046, doi:10.1130/G30331A.1.

Wray, J. J., S. W. Squyres, L. H. Roach, J. L. Bishop, J. F. Mustard, and E. Z. Noe Dobrea (2010), Identification of the Ca-sulfate bassanite in Mawrth Vallis, Mars, *Icarus*, *209*(2), 416–421, doi:10.1016/j.icarus.2010.06.001.

Xu, W., N. J. Tosca, S. M. McLennan, and J. B. Parise (2009), Humidity-induced phase transitions of ferric sulfate minerals studied by in situ and ex situ X-ray diffraction, *Am. Mineral.*, *94*(11–12), 1629–1637, doi:10.2138/am.2009.3182.

Xu, W., J. B. Parise, and J. Hanson (2010), $(H_3O)Fe(SO_4)_2$ formed by dehydrating rhomboclase and its potential existence on Mars, *Am. Mineral.*, *95*(10), 1408–1412, doi:10.2138/am.2010.3470.

Yen, A. S., et al. (2008), Hydrothermal processes at Gusev Crater: An evaluation of Paso Robles class soils, *J. Geophys. Res.*, *113*, E06S10, doi:10.1029/2007JE002978.